Title

Calibration of Scintillation Detectors in the MEG II Experiment

Author

Milgie, Michael James

Publication Date

2019

UNIVERSITY OF CALIFORNIA,
IRVINE

Calibration of Scintillation Detectors in the MEG II Experiment

Thesis

submitted in partial satisfaction of the requirements
for the degree of

MASTER OF SCIENCE

in Physics

by

Michael James Milgie

Thesis Committee:
Professor Peter Taborek, Co-Chair
Professor William R. Molzon, Co-Chair
Professor Zuzanna Siwy

2019

DEDICATION

For family and friends

TABLE OF CONTENTS

Page

LIST OF FIGURES iv

LIST OF TABLES vi

ACKNOWLEDGMENTS vii

ABSTRACT OF THE THESIS viii

CHAPTER 1: An Overview 1

CHAPTER 2: Scintillation Detector Alignment System: Overview and Constraints 9

CHAPTER 3: Scintillation Detector Alignment System: Characteristic Properties 14

CHAPTER 4: Position Crosscheck Using External X-ray Detectors 24

CHAPTER 5: Experimental Results and Conclusion 39

APPENDIX A: Quadrant Photodetector Calibration 47

APPENDIX B: Alignment Procedure 54

APPENDIX C: Electrical Connections 60

APPENDIX D: Detailed Drawings 62

BIBLIOGRAPHY 67

LIST OF FIGURES

Page

Figure 1.1 Standard Model Michel Decay of Muons 2

Figure 1.2 $\mu^+ \Rightarrow e^+ \gamma$ Decay Modes 3

Figure 1.3 MEG Beam Transport System 4

Figure 1.4 Upgraded MEG II Overview 5

Figure 1.5 PMT vs MPPC Gamma Detection 7

Figure 2.1 Alignment Device Sketch 12

Figure 2.2 Detailed Alignment Device 13

Figure 3.1 Four quadrant photodetector output 15

Figure 3.2 Four quadrant photodetector best fit lines 15

Figure 3.3 Four quadrant photodetector raw output 17

Figure 3.4 Four quadrant photodetector normalized output 17

Figure 3.5 Horizontal variance of quadrant photodetector in mm 18

Figure 3.6 Vertical variance of quadrant photodetector in mm 18

Figure 3.7 Explanation of pitch perturbation 19

Figure 3.8 Plot of characteristic yaw 20

Figure 3.9 Plot of characteristic pitch 21

Figure 3.10 FEA of I beam 22

Figure 3.11 Roll monitoring system 23

Figure 4.1 X-ray detector design 26

Figure 4.2 X-ray detectors 27

Figure 4.3 X-ray detector drawing 27

Figure 4.4 X-ray detector experimental setup 28

Figure 4.5 LYSO X-ray detector signal detection 29

Figure 4.6 LYSO X-ray detector characteristic background 30

Figure 4.7 BGO X-ray detector background 31

Figure 4.8 BGO X-ray detector signal 32

Figure 4.9 X-ray detector light leak 33

Figure 4.10 X-ray detector no optics grease 33

Figure 4.11 X-ray detector with optics grease 34

Figure 4.12 LYSO X-ray detector background vs signal 35

Figure 4.13 Lead collimator results 37

Figure 5.1 Alignment device mounted in COBRA 39

Figure 5.2 Enhanced view alignment device mounted in COBRA 40

Figure 5.3 LYSO X-ray detector mounted in COBRA and near LXe 42

Figure 5.4 WaveDREAM LYSO X-ray detector background 43

Figure 5.5 WaveDREAM LYSO X-ray detector signal 44

Figure 5.6 Lead attenuators installation 45

LIST OF TABLES

Page

Table 2.1 Attenuation Length Vs Energy 10

Table 2.2 Average transmission of radioactive cobalt 11

Table 4.1 Collimator results 36

ACKNOWLEDGMENTS

I would like to thank Professor Bill Molzon for allowing me the excellent opportunity to work on this delightful project. It has been helpful to substantially improve my engineering skillset, reinforce my physics background, and introduce me to the exciting field of particle physics. I am grateful for his guidance, help, and oversight through the entirety of this project. I further wish to thank him for allowing me the opportunity to recruit and manage a team of undergraduate students to assist with the project. I have grown as a person and scientist while working under his tutelage.

I would also like to thank Professor Taborek for allowing me the opportunity to gain experience in experimental particle physics and be the co-chair for this thesis. I also wish to thank him for being on my advancement committee, and the chair of my PhD work.

I would like to thank Professor Chanan for allowing us to use his lab and optics bench to calibrate our alignment device.

I would like to thank my undergraduate professors Dr. Vaman Naik, Dr. Ratna Naik, and Dr. Jin Wang; for introducing me to experimental scientific research, and igniting my passion for it.

I would like to thank the post-docs; Dr. Terence Libeiro, and Dr. Yumei Zhang, for their guidance and support throughout this project. It would not have been possible without their efforts.

I would like to acknowledge and thank my undergraduate students Ying Jin, Aaron Esparza-Almaraz, and Danny Lin. They were of great assistance in helping this project stay ahead of schedule and be completed on time.

Mark Steinborn and the UCI Physical Sciences Machine shop are acknowledged for assistance in fabrication of tools, along with Jeff Griskevich and the Physical Sciences High Bay. Their help has substantially improved my machining capabilities.

I would also like to thank Ferdinand Badescu and Benjamin Avila for their assistance in learning to fabricate PCBs. I have found this to be a useful and enjoyable addition to my skillset.

Lastly, I would like to thank and acknowledge the support, encouragement, and advice provided by all of the above, along with my family, and many other graduate students and professors. Thank you for pushing me to pursue my passion.

ABSTRACT OF THE THESIS

Calibration of Scintillation Detectors in the MEG II Experiment

By

Michael James Milgie

Master of Science in Physics

University of California, Irvine, 2019

Professor Peter Taborek, Co-Chair
Professor William R. Molzon, Co-Chair

The Mu to E Gamma (MEG) II experiment is designed to increase the sensitivity of the original MEG experiment by an order of magnitude in the search of the $\mu^+ \Rightarrow e^+ \gamma$ decay that violates lepton flavor conservation, which is not allowed [1]. The final results of the original MEG experiment at the Paul Scherrer Institut (PSI) during the period of 2009-2013 produced 7.5 x 10^{14} muons stopped on target, and put a new upper limit on the branching ratio of this decay of $\beta(\mu^+ \Rightarrow e^+ \gamma) < 4.2 \times 10^{-13}$ [2]. The MEG II upgrade features the world's most intense DC muon beam, innovative liquid xenon tank (LXe) γ-ray detectors, and many sophisticated calibration methods [3,4]. One vital method being implemented to calibrate the 4092 scintillation detectors inside the LXe is the use of our novel X-ray beam. Two additional methods have been introduced to crosscheck the alignment of the LXe detectors. In this thesis we present an overview of the MEG II experiment, the constraints on our alignment device, the design, alignment procedure, and results of this new calibration device.

Chapter 1

An Overview

The purpose of the MEG II experiment is to detect, or put a new upper limit on the branching ratio of the $\mu^+ \Rightarrow e^+ \gamma$ decay. The Standard Model (SM) even with the inclusion of neutrino mass and mixing predicts this decay is experimentally unobservable, with a branching ratio of ~ 10^{-55} given by [3, 5, 6]

$$\mathcal{B}\left(\mu^+ \to e^+ + \gamma\right) = \frac{3}{32} \cdot \frac{\alpha}{\pi} \cdot \left(\frac{\Delta m^2}{M_W^2}\right)^2 \cdot \sin^2(\theta_1) \cdot \cos^2(\theta_2)$$

where Δm^2 is the μ^+ - e^+ type neutrino mass difference, M_W is the mass of the W-boson, and the θ terms are the mixing factors in the neutrino mass matrix. This predicted branching ratio is many orders of magnitude smaller than the reachable sensitivity of any experiment.

$$\begin{aligned}\mathcal{B}\left(\mu^+ \to e^+ + \gamma\right) &= 5 \cdot 10^{-48} \cdot \left(\Delta m^2/\mathrm{eV}^2\right)^2 \cdot \sin^2(\theta_1) \cdot \cos^2(\theta_2) \\ &\approx 10^{-55}.\end{aligned}$$

The SM of particle physics has been very successful, and was able to predict certain particles before they were actually observed. However, the SM does not explain all open questions of particle physics. For example, the SM cannot describe gravitation, or explain what dark matter is. Furthermore, recent experiments have shown that neutrinos have a tiny, non-vanishing mass, these are responsible for the extremely small prediction above. The observation of charged lepton flavor violation would be a clear signal of non-trivial physics beyond the standard model.

Most models beyond the SM allow lepton flavor violation with a much larger branching ratio as big as ~10^{-13} [1, 7, 8, 9, 10]. Thus the MEG II experiment will either observe the

$\mu^+ \Rightarrow e^+ \gamma$ decay and prove the existence of new physics beyond the SM, or put a stringent constraint on the allowed parameter space of new theories. To search for such a violation, the MEG II experiment observes the decay of anti-muons. These subatomic particles have a mean lifetime of ~2.2 μs and are known to decay into a positron, electron neutrino, and muon antineutrino as can be seen in the Feynman diagram below in Figure 1.1.

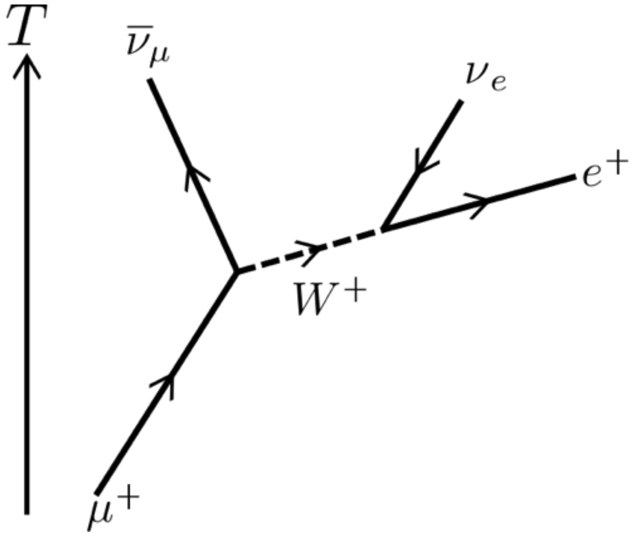

Figure 1.1: The dominate muon decay mode can be seen above known as the Michel decay. Neutrino-less decay modes are kinematically allowed, but are forbidden in the Standard Model due to lepton flavor conservation [11].

A negatively charged muon would simply be captured by nuclei at the stopping target, however positively charged muons are used for the MEG experiment. The positive muon beam is stopped in a target and the muons decay at rest. The signature of the $\mu^+ \Rightarrow e^+ \gamma$ decay is characterized by three factors. The energies of the emitted positron and photon are equal to half of the muon mass, with both having energies of 52.8 MeV. Second, the positron and photon must be emitted back-to back. Lastly, the positron and photon are emitted coincident in time. The Feynman diagrams contributing to the $\mu^+ \Rightarrow e^+ \gamma$ decay can be seen below in Figure 1.2 [5].

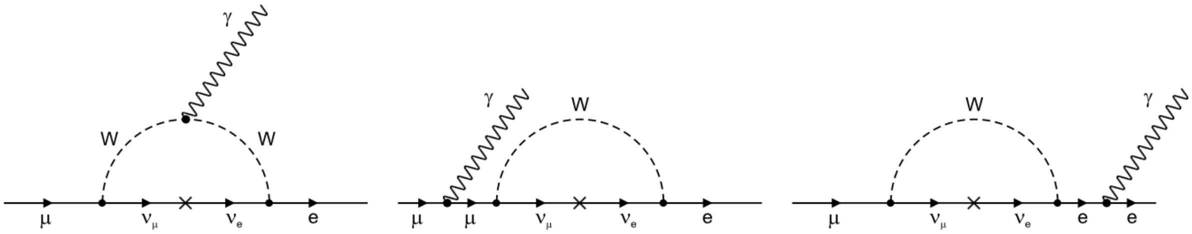

Figure 1.2: The three possible decay modes for the $\mu^+ \Rightarrow e^+ \gamma$ decay can be seen above in the SM with neutrino oscillations. Figure reproduced with permission [5].

There are two types of background events detected by the MEG experiment. The first is a radiative muon decay, where the neutrinos carry away some small energy. This type of background is not a serious problem for the MEG experiment, as detector resolutions can differentiate this background from a signal. The second kind of background events are accidental coincidences of a positron from a Michel decay, and an overlapping photon with an energy of 52.8 MeV from another source. This source could be from radiative muon decays, annihilation-in-flight, or bremsstrahlung of positrons from Michel decays. These accidental coincidences are the dominant background for the MEG experiment and set a limit on the possible sensitivity [1, 12].

Muons are produced for the experiment using the world's most intense DC proton accelerator at the Paul Scherrer Institut. The beam transport system, seen below in Figure 1.3 produces the most intense source of continuous muons in the world. The system is capable of delivering more than 10^8 $\mu+/s$ at 28 MeV/c to the MEG experiment. The optimal rate of muons for the experiment has been determined to be 3 x 10^7 Hz due to limitations of the tracking system, limited by the accidental background [2, 4].

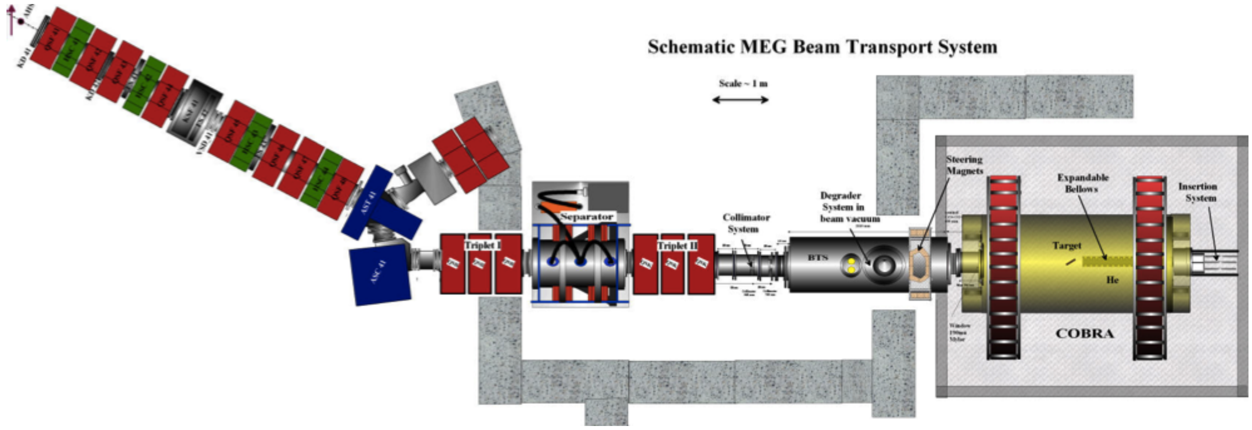

Figure 1.3: The left portion of the apparatus depicts the π*E*5 channel which connects to the MEG beam line starting at the extraction element Triplet I exiting the wall. The beam then goes through a separator and collimator system to eliminate beam contamination. The final beam adjustment and focusing are performed in the superconducting solenoid beam transport system, before the muons are finally stopped by an ultra-thin target placed at the center of the COBRA (constant bending radius magnet) positron spectrometer [4].

The muons produced strike a 140μm thick stopping target made of an elliptical shaped sheet of polyethylene foil, angled at 15°. The target is optimized to maximize stopping efficiency, while also minimizing multiple interactions, bremsstrahlung, and the annihilation-in-flight (AIF) of positrons from muon decays [2]. The COBRA magnet has a graded magnetic field ranging from 1.27T at the center to 0.49T at the far end and is designed so that positrons emitted from the target follow a trajectory with a near constant bending radius [2, 13]. Thus muon stops in the target, and decays into a positron, which is then detected using drift chambers in the COBRA. The liquid xenon tank, equipped with over 4000 detectors can then detect if a gamma ray was emitted. An overview of the COBRA and scintillation detectors can be seen below in Figure 1.4.

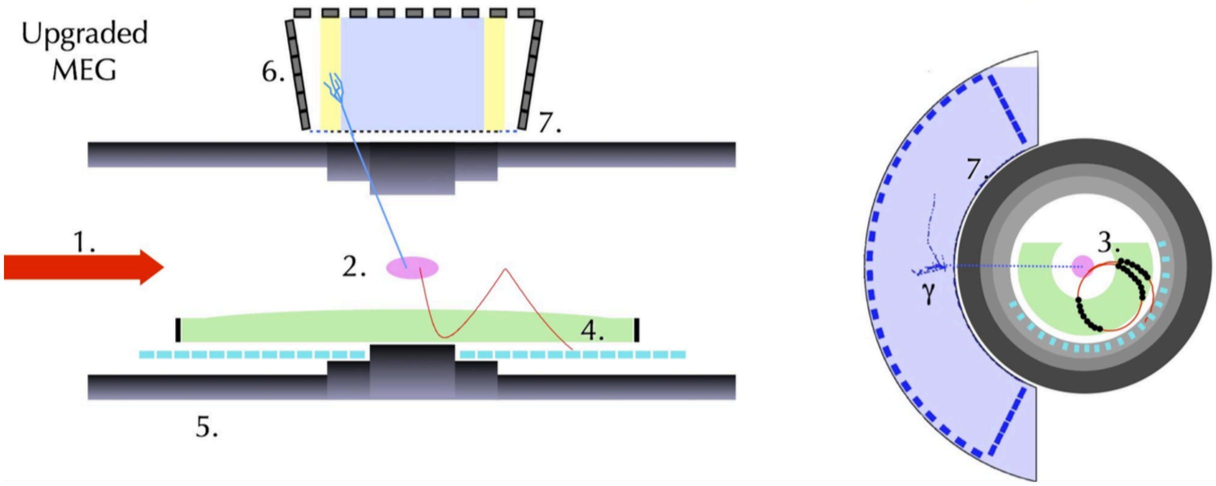

Figure 1.4: The diagrams above depict the incoming muon beam (1) striking the stopping target (2). At the target, the muon decays into a positron (3), which is detected in the drift chamber (4), and a gamma ray which is detected in the LXe. Inside the LXe the gamma ray is detected via photomultiplier tubes (PMTs) (6), and multi-pixel photon counters (MPPCs) (7) [12].

As the continuous beam of positive muons enters the COBRA, roughly 80% of the muons lose their kinetic energy and come to rest inside the stopping target [2]. Since energy and momentum must be conserved, the positron and gamma ray must leave the target in opposite directions, each with half the rest energy of the muon. To observe and measure these events, three detectors are used: a drift chamber to measure positron trajectory and momentum, a timing counter to measure positron time, and the LXe to measure the gamma ray time, position, and energy [2, 14, 15, 16]. Data from all three detectors must be used to get a complete picture of each muon decay and determine if a $\mu^+ \Rightarrow e^+ \gamma$ decay is observed.

The LXe photon detector requires excellent time, position, and energy resolutions to detect a characteristic $\mu^+ \Rightarrow e^+ \gamma$ decay, and distinguish it from background signals [1, 2, 17, 18]. The calorimeter is able to fully contain and measure the shower induced by a 52.83 MeV gamma ray with high efficiency [2]. The photon is not measured directly by the LXe, but rather the xenon is used as a scintillation material, and the phonons produced by this scintillation are detected by a large array of Hamamatsu MPPCs on the interior of the cryostat. Liquid xenon was chosen as the scintillation material because it has a high density, and short radiation length, thus making it an efficient detection medium for photons [2, 19, 20, 21].

A scintillating material has a luminescence property when excited by ionizing radiation. Xenon is widely used as a detector material in different fields because it produces scintillation photons in response to radiation [22, 23]. Gamma rays around 50MeV interact with the xenon primarily through pair production [24, 25]. The high density and large atomic number allow LXe to efficiently detect gamma rays. It is further suitable for measurement in a high rate environment. In addition, since scintillation light is emitted only by the excited dimer (Xe_2^*), xenon scintillation photons cannot be re-absorbed by LXe [26]. This is a major advantage and allows for the high energy resolution achieved by the detector. Xenon also can be purified at any point, this is not possible with crystal scintillators [27, 28]. For all of these reasons it was concluded that LXe was the best scintillator for the gamma-ray detector. To achieve a high acceptance for gamma ray detections, the LXe is the largest in the world, with a volume of near 900L [1, 2].

To achieve the precision necessary to increase the upper limit on the branching ratio for the MEG II experiment the photon detection system inside the LXe was upgraded. In the original MEG experiment an array of 846 UV-sensitive PMTs were used to detect a potential gamma decay [1, 19]. In the MEG II experiment, the front inner wall of the LXe has been upgraded to use an array of 4092 MPPCs also known as Silicon photomultipliers (SiPM) to replace the PMT system in use. While the MEG II still contains PMTs on other inner walls of the cryostat, the most vital wall, nearest to the muon beam, was upgraded to provide better positon and energy resolution.

The new Hamamatsu SiPMs have many desirable properties outlined below. The new devices are much smaller than PMTs used in the past, with dimensions of 15mm x 15mm, they are much smaller than the 2-inch diameter PMTs. The active area of these devices were developed to be 12mm x 12mm, leaving the majority of the LXe inner surface capable of detecting scintillation photons. This increases the precision of photon detection, especially when an array of these targets is used. Further, the new SiPMs are sensitive to a single photon, have high photon detection efficiency, are insensitive to the strong magnetic field around the COBRA magnet, have excellent time resolution (<100ps), and low power consumption [20]. A figure depicting the difference in PMT and MPPC detection can be seen below in Figure 1.5.

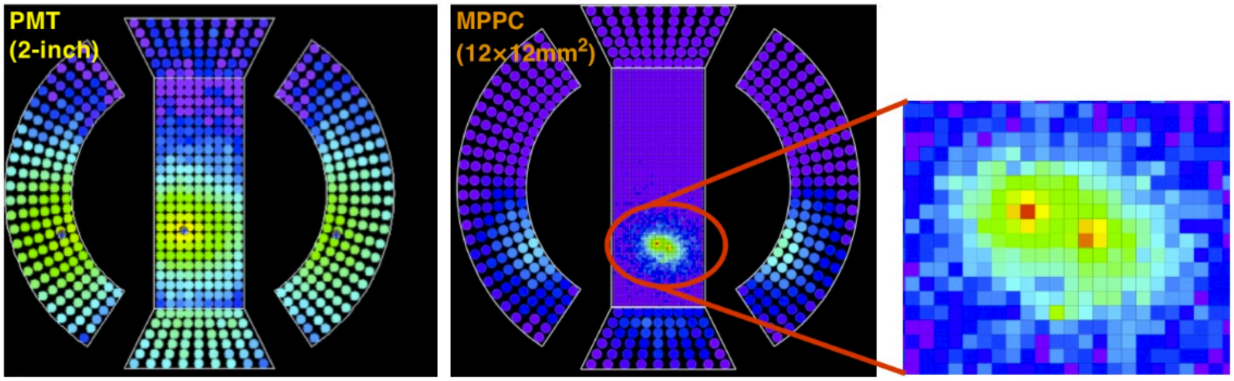

Figure 1.5: Typical output of scintillator light distribution from gamma rays can be seen above. The larger PMTs on the left, and much smaller new MPPCs on the gamma entrance face can be seen on the right [4].

The large array of the 4092 Hamamatsu MPPCs was installed, and their positions were determined using a FARO measuring device [2, 21]. The MPPCs are mounted on a PCB strip containing 44 MPPCs in a line along the Z direction, with an array of 93 strips total. It is important that these strips are precisely aligned on the inner wall, and to minimize the gap between the LXe wall and PCB. Any LXe found in this gap deteriorates gamma ray detection efficiency, and causes an undesirable low energy tail in the energy response function of the detector. Even small distortions in the PCB strip could therefore be an issue. Motion of the MPPCs during cooldown due to contraction and buoyant forces must also be considered to minimize experimental uncertainty. To insure proper alignment and functionality of the vital LXe photo detection system we have been tasked with alignment of the 4092 MPPCs.

The MEG II experiment will be fully operational and begin taking data sometime in fall of 2019. The experiment is expected to explore the $\mu^+ \Rightarrow e^+ \gamma$ decay down to a branching ratio of 5 x 10^{-14} over the next few years [3]. Observation of this decay would be an unambiguous signature of new physics, while improvements on the current limit will stringently constrain many of the new models beyond the SM.

Chapter 2

Scintillation Detector Alignment System: Overview and constraints

The goal of this project is to align the LXe detectors using X-rays via in-situ measurement of all 4092 MPPC positions in a fully operational configuration. A technique that does not require beam time, takes modest time for measurement, and is repeatable is desired. The method being implemented must allow for crosschecks using optical survey allowing direct correlation between LXe and drift chamber alignment. To achieve these goals a collimated X-ray beam of known position and orientation will be used. Other constraints on the system are a small X-ray beam in comparison to the MPPC dimensions, sufficient rate to decrease measurement time, high precision beam alignment, a large enough X-ray energy to have a high transmission probability into the liquid xenon tank, and a low enough energy that the absorption length in LXe is short so photons undergo photoelectric effect directly in front of the MPPC. To achieve these goals a laser alignment system has been mounted on a translational collimator system we built to monitor the position of the beam, as will later be described in more detail. This location is crosschecked using small X-ray detectors on the cryostat exterior. The system is controlled and data is collected using a standard data acquisition (DAQ) device.

The X-ray source options are an X-ray tube or a radioactive source. The advantages of a radioactive source are a mono-chromatic beam, small physical size, and a reasonable rate that can be collimated to a small spot size. An X-ray tube with a roughly 100keV energy is orders of magnitude larger than a radioactive source, and requires roughly 100,000V to power. The energy of the source should be below 200keV to keep interaction in the LXe close to the MPPC, and above 100keV to allow for an acceptable transmission rate through the COBRA and into the

LXe cryostat. Radioactive cobalt 57 has an x-ray energy of 122keV and has been chosen to serve this purpose. ^{57}Co has a half-life of 271.8 days so it is important to fabricate the source near the time it is to be used in the MEG II alignment. This isotope is produced by cyclotron irradiation of iron and the principle reaction can be seen below [22].

$$^{56}\text{Fe} + {}^{2}\text{H} \rightarrow \text{n} + {}^{57}\text{Co}$$

The COBRA and entrance to the LXe were designed to minimize attenuation of 53 MeV photons. The LXe wall is composed of a thin layer of stainless steel (0.5mm), and 2mm of carbon fiber allowing a mechanical strength of up to ~3 atm. The COBRA is the largest source of attenuation with ~7mm of aluminum and ~1mm of superconductor in copper from the coils used to produce the magnetic field [12]. X-rays are absorbed as they pass through materials according to the exponential law $I = I_0e^{-\mu d}$ where I is the reduced intensity, I_0 is the incident intensity, μ is the material dependent absorption coefficient, and d is the distance traversed through the material. Typical attenuation lengths can be seen below in Table 2.1 for various energies in aluminum and xenon.

Energy [keV]	Attenuation length [mm]	
	aluminum	xenon
50	10.1	0.26
75	17.1	0.76
100	21.8	1.65
125	24.5	2.86
150	26.5	4.6
250		13.2
500		34

Table 2.1: The attenuation length of various energies in aluminum and xenon can be seen above. Xenon is a much more efficient attenuator than aluminum, allowing for our radioactive signal to be scintillated near the surface of the MPPCs.

COBRA winding				Cobra cryostat	Lxe front cryostat		
thickness [mm]	Cu [mm]	Al [mm]	total average trans.	trans.	0.5 mm steel trans.	2.0 mm carbon trans.	average trans.
8.500	1.215	7.285	0.525	0.822	0.901	0.953	0.371

Table 2.2: The COBRA attenuates nearly half of our 122 keV source from the copper and aluminum used to construct the magnet. The LXe wall of the cryostat then further attenuate the signal another 15%. It can be seen above that the average transmission of our radioactive source after going through the COBRA and LXe is roughly 37%. The X-rays that do transmit into the LXe topically interact within ~2.8mm of the MPPC array.

A collimator with a slit of dimensions 5mm x 0.15mm x 8cm long has been chosen to illuminate 1 coordinate at a time in the measurement direction and 3 MPPCs in the non-measurement direction. This collimator produces a beam that is 1mm wide at the MPPCs in the measurement direction. In order to increase the data rate, the calibration system we have designed scans the LXe in steps of 1/10th of the MPPC size in the measurement direction. To cover the entire array of MPPCs in the calorimeter a translational stage with a Z motion of at least 600mm is required. A rotational stage is also required on the translational stage to cover the full ϕ extent of the calorimeter. An accurate location of the radioactive source is required with respect to the LXe to accurately measure the location of the MPPCs with respect to the beam line. To measure the precise location of the radioactive source a survey will be done on site using the FARO measuring tool. Further, a laser and detector system is used to monitor slight variations in the pitch and yaw of the source. A level and camera system is implemented to detect variations in the roll of the source over the full translation of the calorimeter.

To achieve all of the aforementioned goals a Standa 8MT295Z-740 motorized linear translational stage has been purchased to translate the source a full distance in the Z direction of 740mm. This device has been mounted in a 3-meter-long I beam with a cutout located off center as seen in figure 2.1. Three adjustable feet and four mounting bolts are used to position and adjust the translational table onto the I beam. The entire I beam is mounted on three more adjustable feet to further assist in leveling the entire system. A three-point mount system has been implemented to reduce torque on the system and deflection of the beam near the center. A three-point system also minimizes deflection of the source as it translates over the beam.

Mounted on the translational stage is a rotational support stage that acts as a mount for a spirit level, camera system, adjustable laser, and the rotational stage itself. The rotational stage being used is the Standa 8MR190-2-4233 motorized rotation stage. To control both the translational and rotational stages a Standa 8SMC4-USB controller is being used, and is given commands remotely via a Raspberry Pi. To determine the location of the source as it translates an OSI Optoelectronics 4 quadrant silicon photodiode (QPD) amplification module has been mounted onto the I beam. This QPD is used to monitor tilts of the stage as in moves in Z. A rough diagram is seen below in figure 2.1, and a picture is seen in figure 2.2.

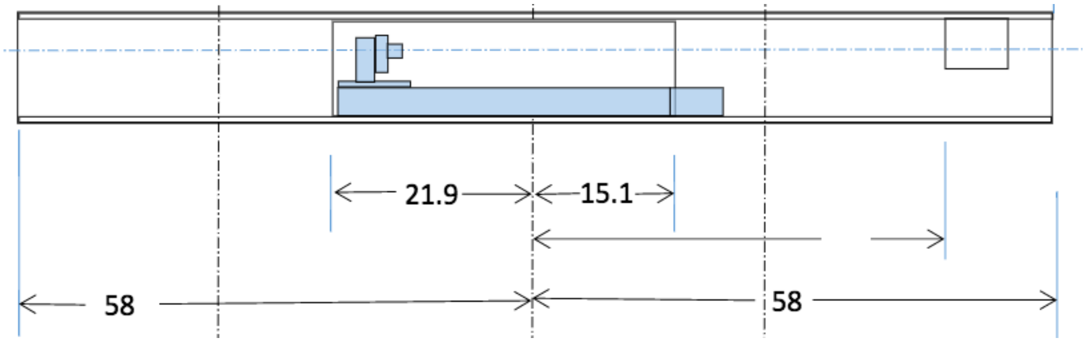

Figure 2.1: A rough sketch of the I beam can be seen above with the relative location of the translational table and rotational stage (in blue). The cutout on the right side is to allow space for the 4 quadrant photodetector, all distances are in inches. A more detailed drawing can be found in appendix D.

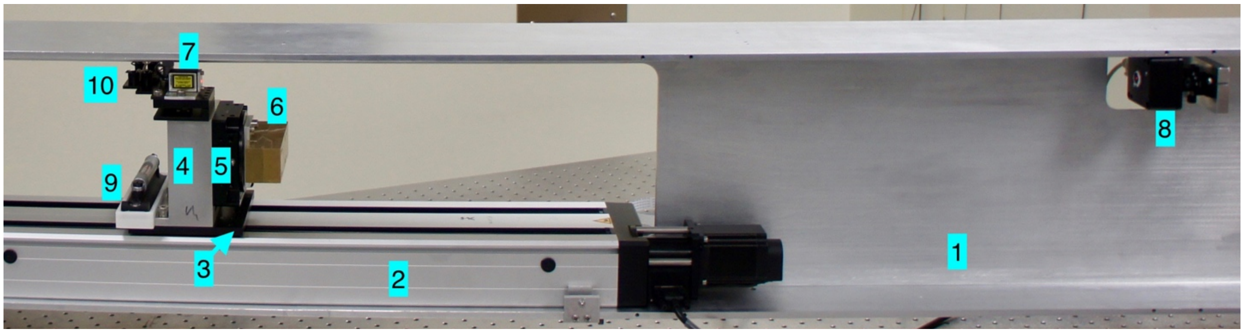

Figure 2.2: The I beam (1) can be seen above with the translational table (2) mounted. On the translational table we see a black mounting stage (3) where the Aluminum rotational support (4) is found. Mounted on this support we see the black rotational stage (5), where the brass collimator (6) is mounted. At the top of this system we see the laser (7) used to provide the location of the collimator. On the right we see the four quadrant photodetector (8) housed in a black box that allows precision translation in both the x and y directions and is used to measure the pitch and yaw of the collimator. To measure the roll of the system, a bubble level (9) is monitored using a Raspberry Pi camera system (10).

Chapter 3

Scintillation Detector Alignment System: Characteristic Properties

The purpose of the aforementioned equipment and the experimental setup of our calibration device is to ensure we have a well-known location of our radioactive Co-57 source. At each location in Z, our collimator rotates over the full phi range of the LXe to hit the MPPCs at that specific Z position. The origin of our radioactive X-ray laser is well known using an optical survey performed at PSI, and is monitored at each measurement location using our four quadrant photodector laser system. Further, the roll of the system is monitored using a bubble level that is observed using a camera.

Since the translational stage has reproducible oscillations in its' position both in horizontal and vertical directions, a device to monitor these deviations was needed. To solve this issue, we implemented a laser mounted on top of the mount for the collimator, and a photodector to determine the magnitude of these deviations in position. The four quadrant photodector used in our alignment system has an output range from -1000 to +1000 on both axes as can be seen below in figure 3.1 [29]. The method to determine the calibration constants of this device are detailed in Appendix A. Proper alignment of the device and laser are critical to alignment of the scintillation detectors in the LXe. The calibration curves of this device can be seen in figure 3.2 and allow the output intensities to be converted to known distances and therefore deflections from the centerline of the alignment system. These perturbations of the centerline allow us to measure the pitch and yaw of the alignment system.

To determine deflections in the system the relative intensity of the detector was used. This measurement is defined as the division of the output in horizontal or vertical directions, divided by the total intensity of the quadrant photodetector. For example, a typical total intensity output for the detector is usually on the order of +1000. If the laser is slightly off target in the horizontal direction, say by 200, we then divide this output by the total summed intensity output of the device to get a value of 0.2. We then convert these perturbations in x and y to get values for the tilt and yaw of the system.

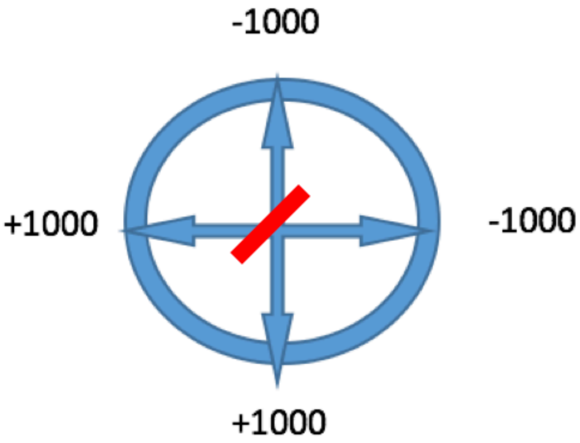

Vertical	**Horizontal**	**Total Intensity**	**Z position (mm)**
-56	**7**	**1019**	**130**

Figure 3.1: A diagram of the coordinates of the four quadrant photodector can be seen above along with a table of typical output values. As the translational table moves the source in Z, a characteristic pattern has been found due to intrinsic properties of the translation table.

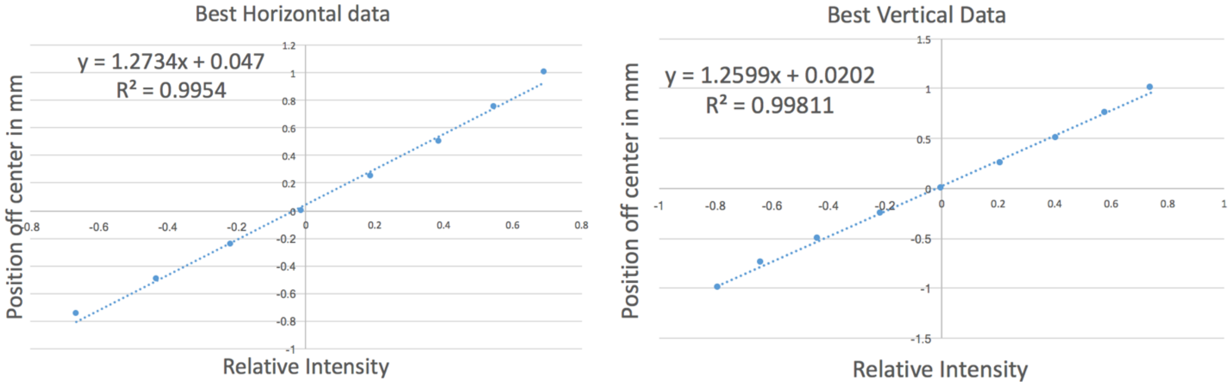

Figure 3.2: The best fit lines for horizontal and vertical calibrations of the quadrant photodetector is displayed. A change in relative intensity of 0.2 correlates to a ~0.27mm translation of the laser.

With the laser mounted on top of the rotational stage, and properly aligned with the quadrant photodetector, the typical output can be seen in figures 3.3 and 3.4 below. Measurements are taken every millimeter, and the raw output is presented. The oscillations in the output seen below have been found to be repeatable. These oscillations are periodic and have been found to be intrinsic to the translational stage's motion. The vertical motion has a periodicity of 10 ± 0.1cm, with peaks found at the Z locations in mm at {55, 154, 255, 354, 455, 553, 654}. The local minimums are also periodic and offset from the peak by 5cm.

The horizontal motion was found to inherently have slightly more variation in the periodicity. This is largely due to the deflection that occurs near the center of motion of the translational table. Nonetheless, the horizontal motion was found to have a periodicity of 10 ± 1cm due to the deflection near the center. For horizontal deflection the peaks were found at Z locations in mm at {69, 164, 261, 383, 466, 567, 667}. Without the center point, the precision of the periodicity is 10 ± 0.5cm. The minimums for the horizontal deflections are just like the vertical minimums and found to be offset from the peak value by 5cm.

These deflections however are not detrimental to determining the position of the 4092 MPPCs we are trying to calibrate. As the laser translates, the deviations will cause the X-ray to be in a slightly different place on the MPPC array. However, since these deviations are monitored via our laser and quadrant photodetector system, we can correlate the displacement of the X-ray beam to the displacement of the MPPC that is hit, and thus still have a valid calibration. The results of this calibration procedure are reproducible and allowed for a precision better than 200 microns.

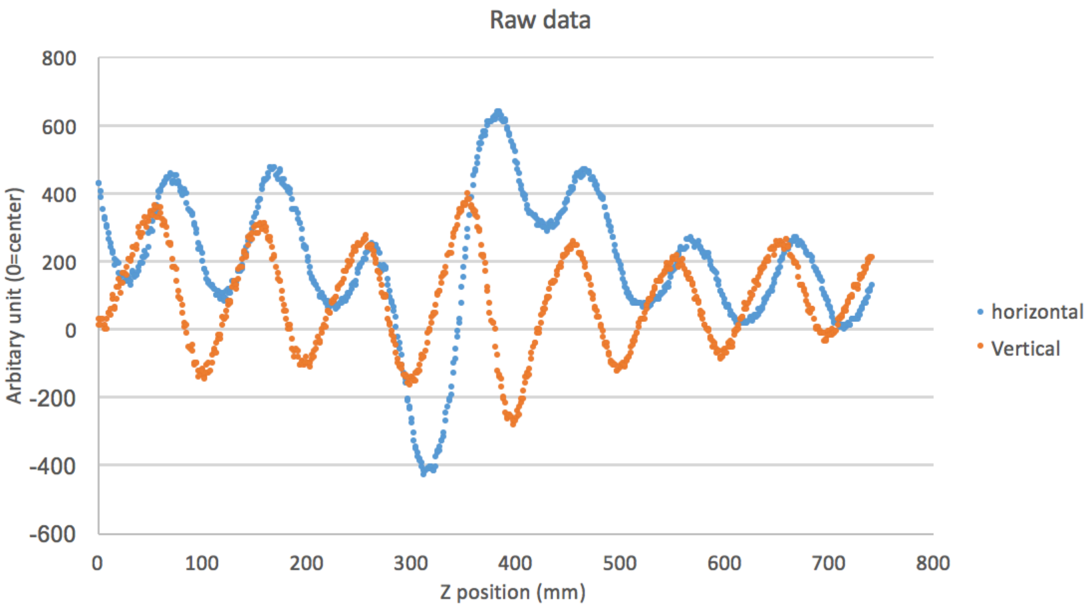

Figure 3.3: The raw data from the photodector and laser alignment system from our calibration device can be seen above. The periodicity of vertical and horizontal data is reproducible and found to occur roughly every 10cm. These perturbations are acceptable for calibration of the 4092 MPPCs as their locations are well known, and can be correlated to deviations detected.

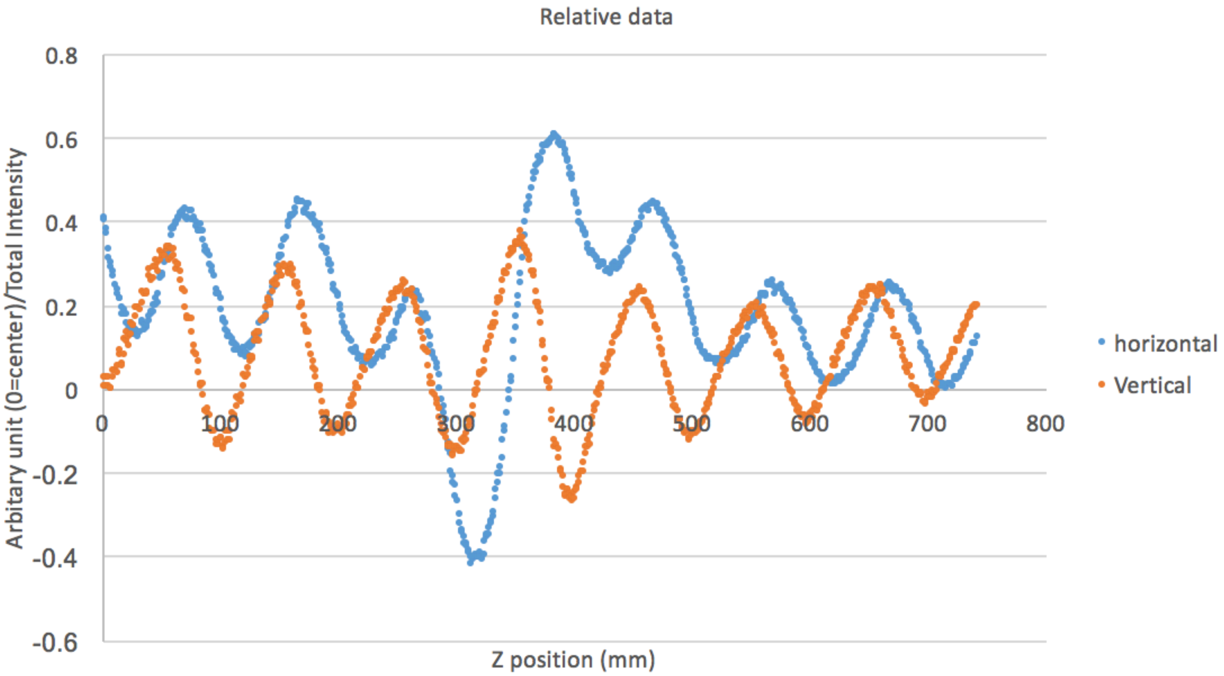

Figure 3.4: Once the raw data is collected, we normalize the data by dividing the horizontal and vertical output by the total intensity detected. The total intensity is typically on the order of 1050 with a max variance of 1.5%.

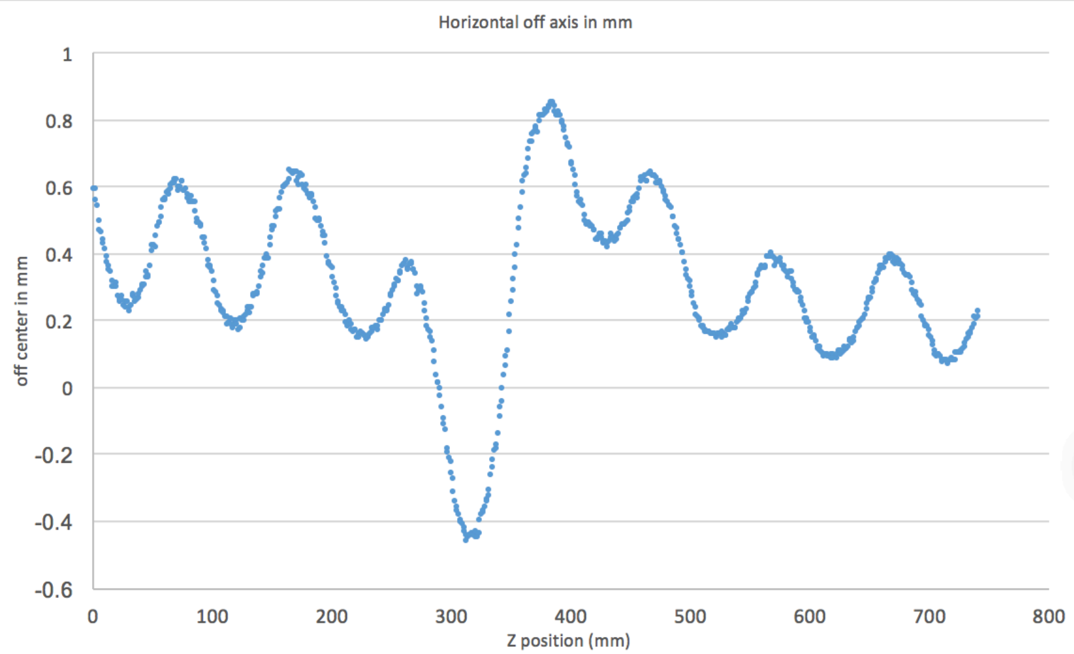

Figure 3.5: Using the aforementioned calibration of the quadrant photodetector, along with the normalized data, the net displacement of the collimator system is plotted above. The maximum variance is found at the center of the translational table, as described by the manufacturer, with a maximum deviation of roughly 1.3mm.

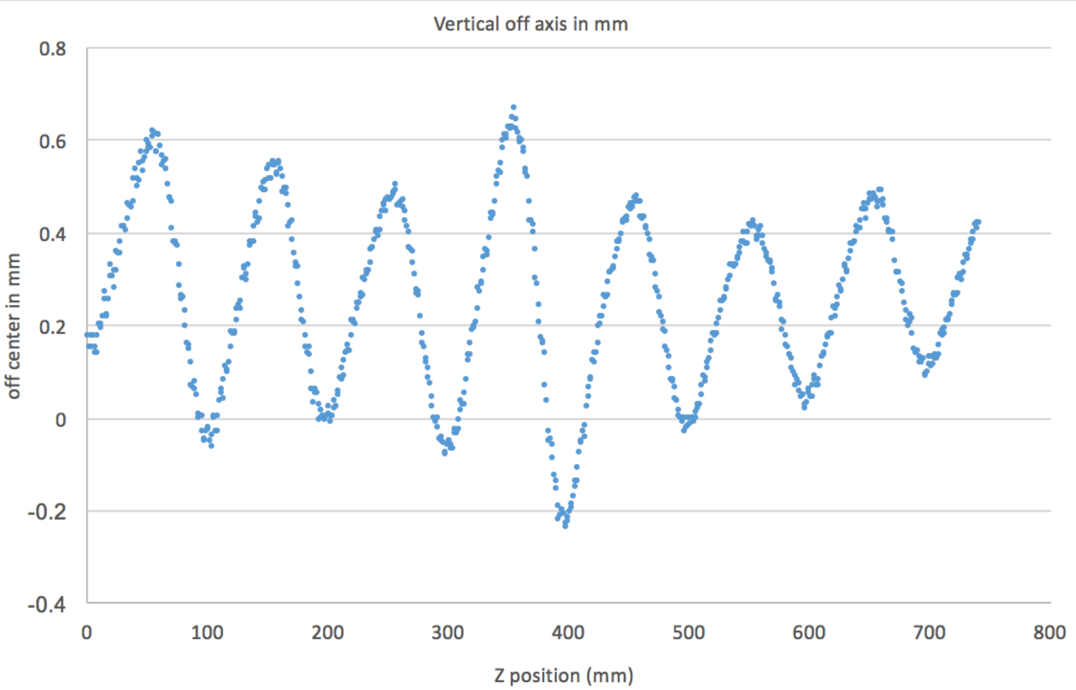

Figure 3.6: Using the same method as above, but with a new calibration constant for the vertical direction, the vertical displacement is plotted above. The periodicity is found to be 10cm, and the maximum displacement has been determined to be 0.9mm.

The perturbations observed above are not direct translations of the collimator system, but rather minor rotations in the pitch and yaw orientations. Since the laser is mounted on top of a translational stage, that is some distance from the pivot point, the perturbations seen above are actually small deflections of the angle of the source. Since the detector is roughly a meter away from the laser, what we are actually seeing is millirad rotations of the source laser as it translates. To determine the angular deflections of the collimator source, we use the distance between the laser source and the quadrant detector, along with the aforementioned calibration of the photodetector (giving the deflection in mm) to determine the angle. A simple diagram of this effect can be seen below.

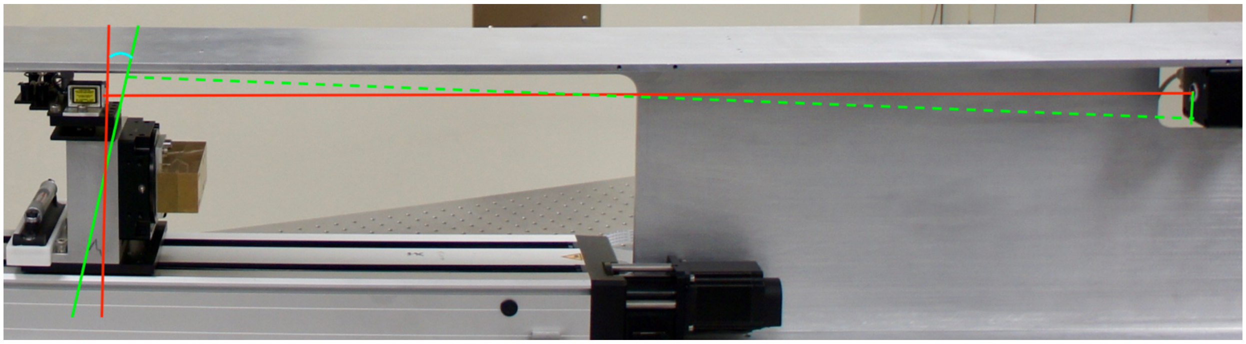

Figure 3.7: An example of a pitch perturbation found in the system can be seen above. The red lines denote the ideal position for the laser, while the green lines mark some exaggerated perturbation in pitch of the system. This pitch produces a deflection from the center on the quadrant photodetector. Since the calibration of the detector is known, along with the distance between the laser and detector, the angle of deflection can be calculated (light blue).

Since the distance between the photodetector and laser is known, along with the perturbed distance detected on the photodetector, the angle that the collimator has been deflected can be calculated. Knowing this angle is important, as it causes a slight deviation in the targeted MPPC. If any of these deviations are detected, we can then check the data collected by the photodector to properly correct the data collected by the MPPC array. The calculation of the angle of the source is simply the inverse tangent of the relative distance between the laser and detector, divided by the displacement detected on the photodetector from the center point. The results from a typical aligned system can be seen below.

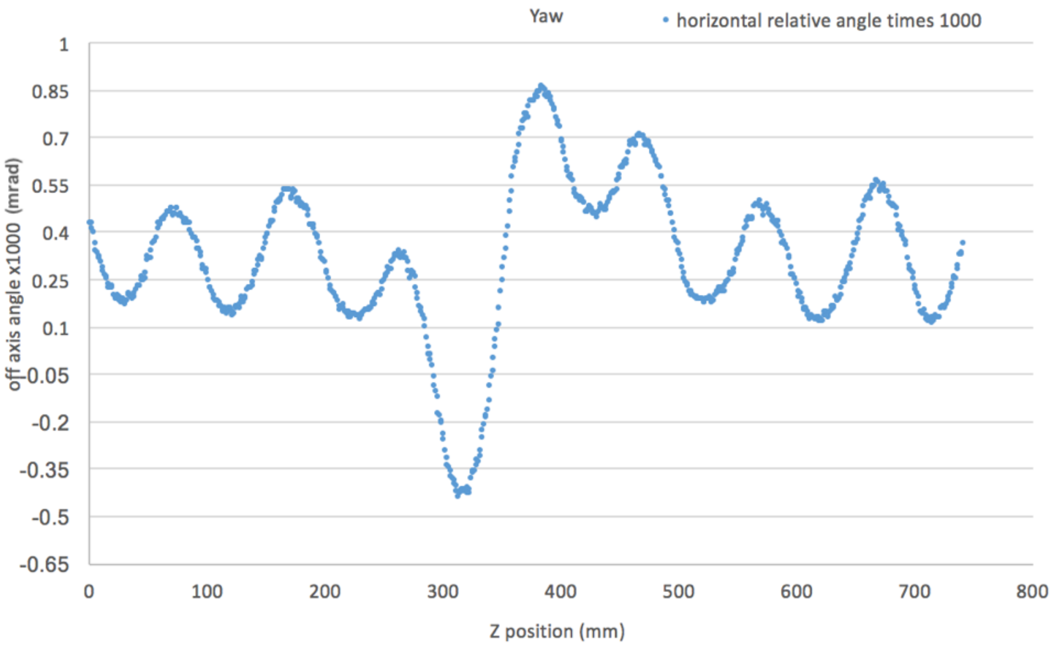

Figure 3.8: The typical yaw inherent to the system is displayed above. The vertical axis is in units of milliradians, and it can be seen the maximum deflection is on the order of 1.3 mrad or 0.075 degrees. The yaw of the system is measured by horizontal deflections on the photodetector.

The yaw found inherent in the system is relatively minor when compared to the MPPC size (12x12mm), the distance between the collimator and MPPC array, and the spot size the collimator produces. The typical pitch found in the system is smaller in magnitude and displayed below. The same method used to measure yaw was implemented to measure the change in pitch of the collimator. The pitch was monitored using the vertical output on the photodetector along with the vertical calibration constant. The characteristic rotations in pitch is plotted below.

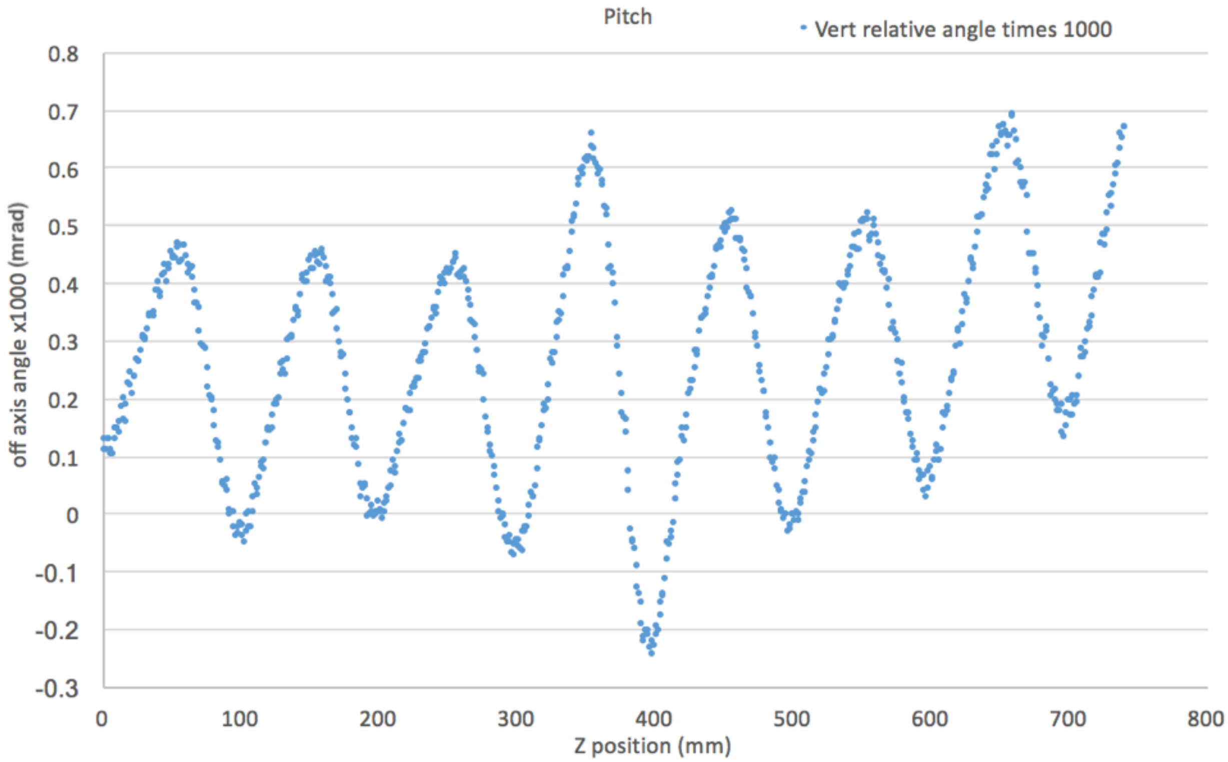

Figure 3.9: Typical results for the pitch angle of the collimator system are displayed above. The maximum deflection is found near the center with a value of 0.9 mrad.

Since minor variances in pitch, yaw, and roll of our alignment system change the position of our x-ray beam, a finite element analysis (FEA) was performed on our I beam, which acts as the support structure for the translational and rotational stages. This was done to determine deflection of the beam at the mounting points for the translational table. The table is mounted using a 3-point support system, as seen in the figure below with orange arrows. As can be seen, the deflection in these regions was found to be minimal, with the greatest deflection occurring at the center of the beam. At the center of the beam, we see a predicted deflection of 0.22mm, however this surface does not directly support the translational stage. At the support points we see a smaller deflection on the order of 0.15mm.

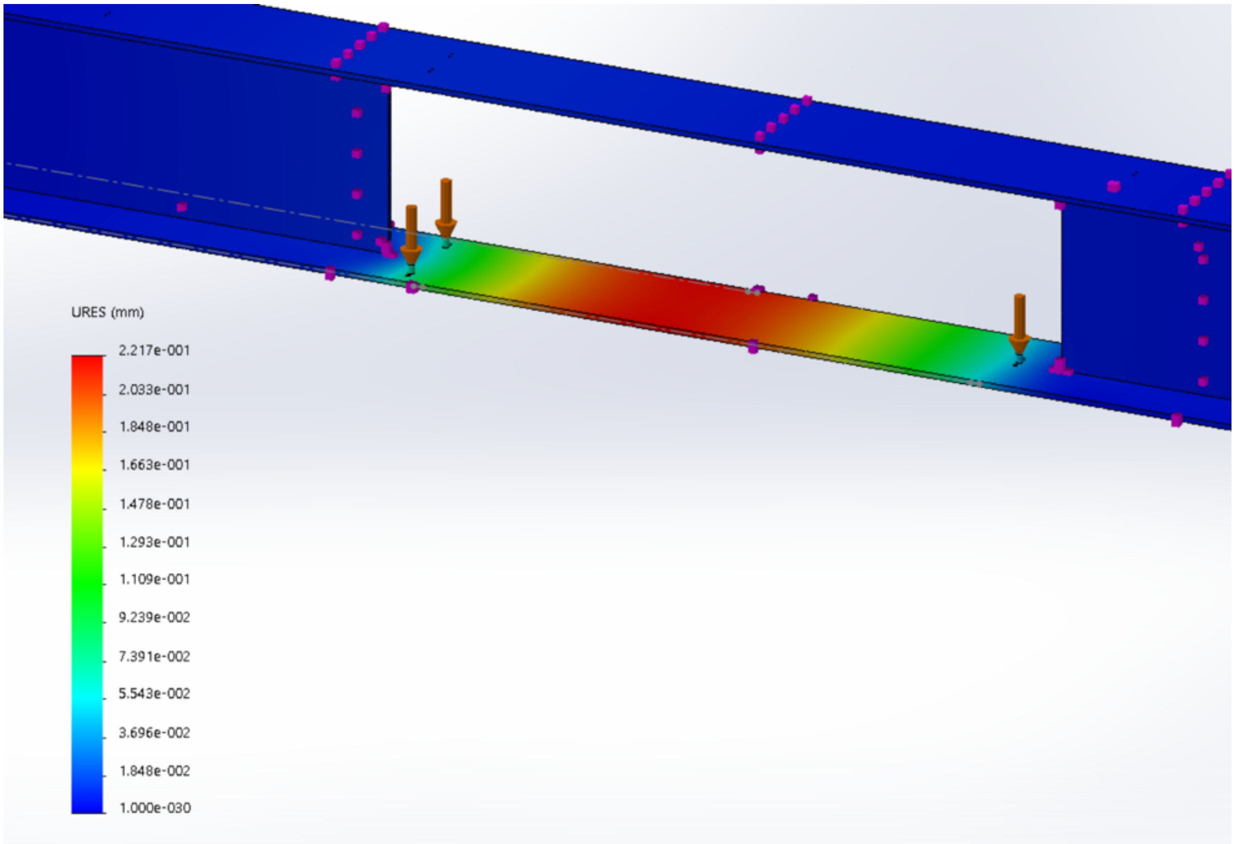

Figure 3.10: FEA was performed on our I beam support structure displayed above. The proper weight was placed on the support locations marked with orange arrows, and the maximum deflection was found. As can be seen, on these support locations, minimal deflection is found. The greatest deflection is found in the middle of the beam cutout, with a value of 0.22mm, however no weight is supported in this region.

The laser and four quadrant photodetector are capable of measuring minor deviations in the pitch and yaw of the alignment device, however do not monitor the roll of the system. To take roll into account, a bubble level with 0.2mrad/tick precision is placed on the base of the translational stage. To record data from this device a Raspberry Pi camera was implemented to take a picture of the bubble level at every location in Z. Since the device will be used in the dark, an LED array was mounted to the camera fixture. These LEDS are powered by the Raspberry Pi. Since the bubble level is so close to the camera, an additional lens was needed to produce a clear image. The roll monitoring system can be seen below in figure 3.11.

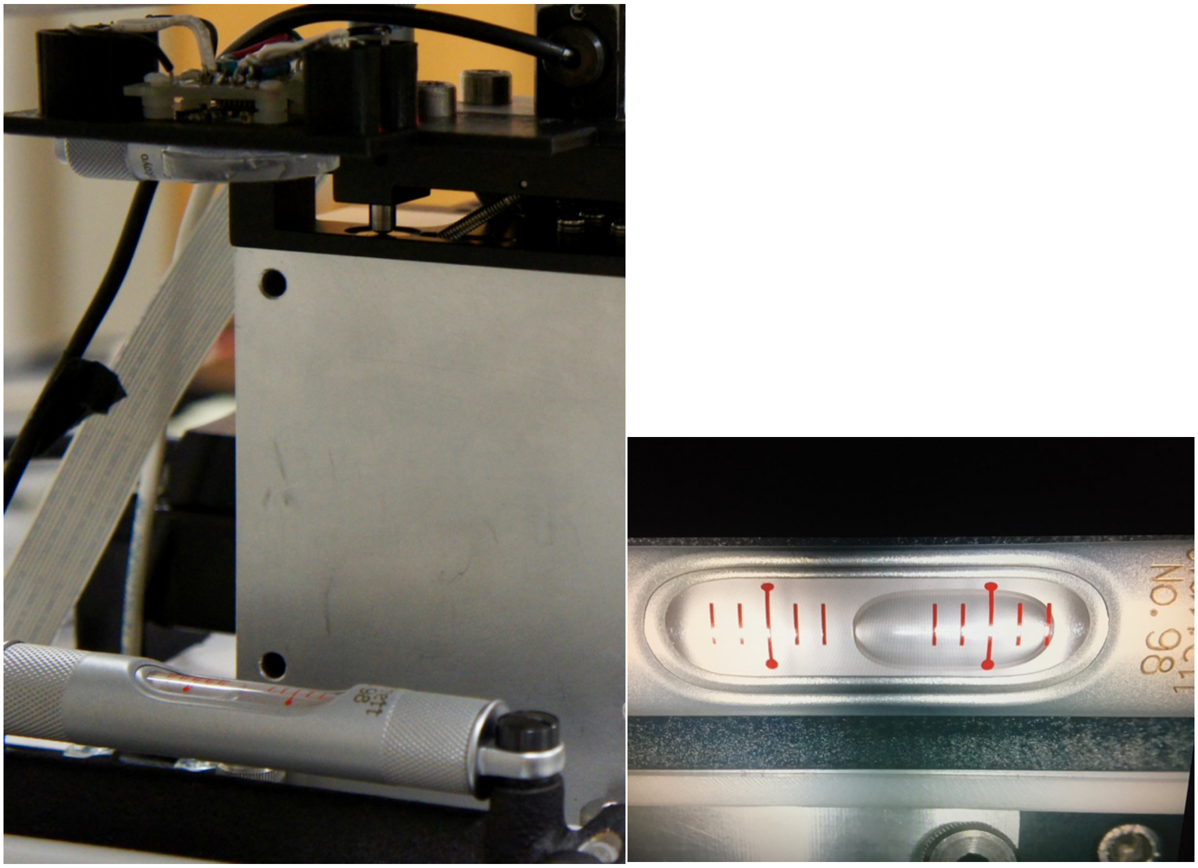

Figure 3.11: The roll monitoring system can be seen above. The camera, lens and LEDs used can be seen near the top of the image on the left. A typical image output from the device can be seen on the right. Each tick on the bubble level represents a 0.2mrad roll.

Typical results found from monitoring the roll of the system were determined to be roughly 1 mrad. The alignment system we produced was found to have relatively minor deviations in all three rotation angles on the order of ~1mrad. These results are consistent with our goal of producing a translational X-ray laser alignment system with a known position of the radioactive source. These results demonstrate the alignment system is capable of producing a calibration of the MPPC array of below the desired 0.2mm precision.

Chapter 4

Position Crosscheck Using External X-ray Detectors

To cross check the position of our radioactive translational X-ray laser alignment device, 6 X-ray detectors have been produced to be mounted on the exterior of the cryostat. The position of these 6 X-ray detectors will be measured via corner cube reflectors and an optical survey. To detect our 122keV X-rays we implement lutetium-yttrium oxyorthosilicate (LYSO) crystals as scintillators, along with a Hamamatsu multi pixel photon counter (MPPC), type S12572-050P to detect the visible light produced by our scintillation crystals. The X-ray detector is housed in a custom 3D printed box made of PLA plastic, and connected to our amplification system and oscilloscope software. The amplifier used is the PSI OG3205 Mar-Amplifier HMF1.0, connected to a computer via the PSI DRS4 Evaluation Board V4, and data is collected via the PSI DRS oscilloscope software. The purpose of this chapter is to describe how the X-ray detectors and related subsystems work, compare the results of LYSO and Bismuth germanium oxide (BGO) crystals, define the properties of these devices, and demonstrate the results and characteristic signal detection of these devices. A video demonstration of our X-ray detector system is also available at the following link. https://youtu.be/KGcYpgu2cWg

The radioactive cobalt source used has an energy of 122keV, this energy correlates to a wavelength of ~10 picometers and can be difficult to detect directly. The Hamamatsu MPPC chosen has a photosensitivity in the region of 300 to 900nm, and thus cannot directly detect the incoming X-rays. In order to detect our radioactive signal a scintillating material and MPPC have been employed similar to the LXe calorimeter. When this material is struck by an incoming electromagnetic wave it absorbs the energy and re-emits some of the energy in the form of visible light. This visible light is then detected by the MPPC as an electron due to the photoelectric effect. For the purpose of this device, the scintillation material must absorb some of the incoming energy, and emit light in the aforementioned 300 to 900nm range. Some scintillation materials can be slightly radioactive in the nanocurie range, and thus produce a background noise detectable by the MPPC due to the close proximity of the crystal and detector. Therefore, a scintillation material must be chosen that has an intrinsic background radiation in a separate region from the radioactive cobalt signal. The scintillation materials tested were both BGO and LYSO crystals, the results from these materials are discussed later. Two different versions of LYSO crystal were tested to compare the effect of reflective coating on 5 edges of the crystal cube, these results are also presented.

The X-ray detector we have designed can be seen below in Figure 4.1, a black PLA plastic 3D printed box houses the scintillation crystal, MPPC, and features two output connections. The scintillation crystals are a cube with dimension of 6.0mm. The dimensions of the device are also seen below in Figure 4.3. The PCB was designed in Easily Applicable Graphical Layout Editor (EAGLE) such that the MPPC is in the center of the board and is symmetric. The 3D printed box is also designed to be symmetric, and as can be seen in the drawing in Figure 4.1 has a curved lid top. The purpose of the curved lid is to conform to the curvature of the exterior of the cryostat. The MPPC has been soldered to the PCB using low temperature thermal paste with a melting temperature of 281^{o}F, and temperature was controlled by using a hotplate set to 300^{o}F. With this temperature the MPPC was successfully mounted to the PCB in ~90 seconds. Optics grease has been used at the interface between the MPPC and scintillator to improve transmission. A comparison with and without optics grease is discussed later in this chapter.

Two connectors were provided for test and normal implementation. To remove the possibility of any external light leaking into the box the X-ray detectors were sealed on top of the PCB and at the exit of the MPPC leads using a black silicon RTV glue.

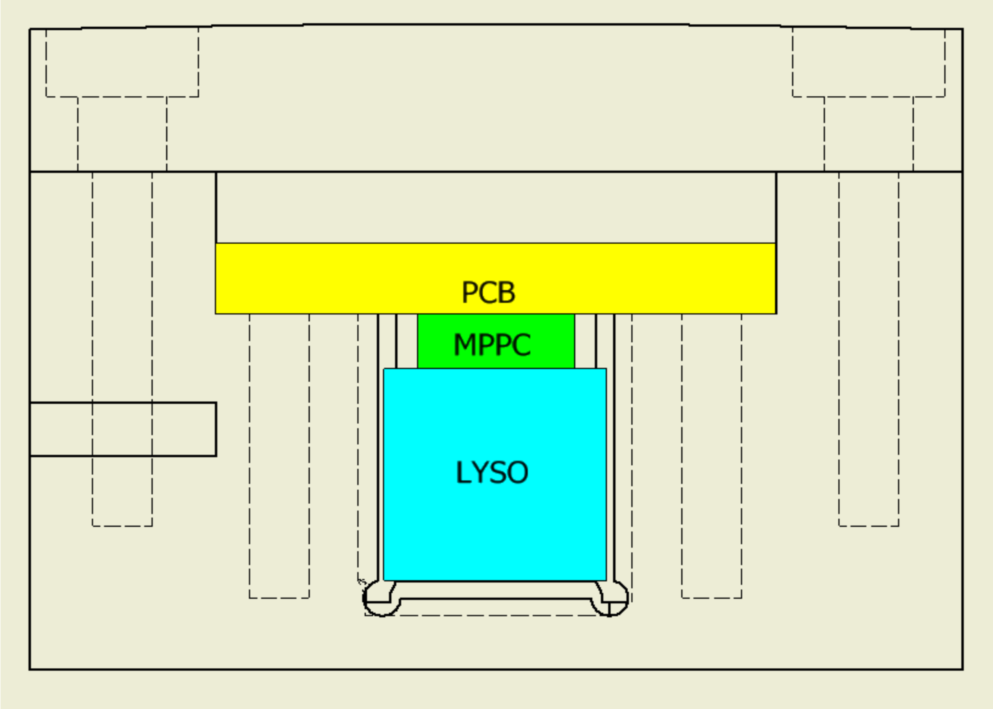

Figure 4.1: A simple drawing of the X-ray detector is shown above. The device is designed symmetrically so that the LYSO crystal and MPPC are at the center of the device. The LYSO crystal fits snuggly in the 3D printed PLA black box so that its' position is well known. The curved lid is designed to fit snuggly against the external wall of the MEG II cryostat. Black silicon RTV seals the components and prevents any external light from leaking into the device.

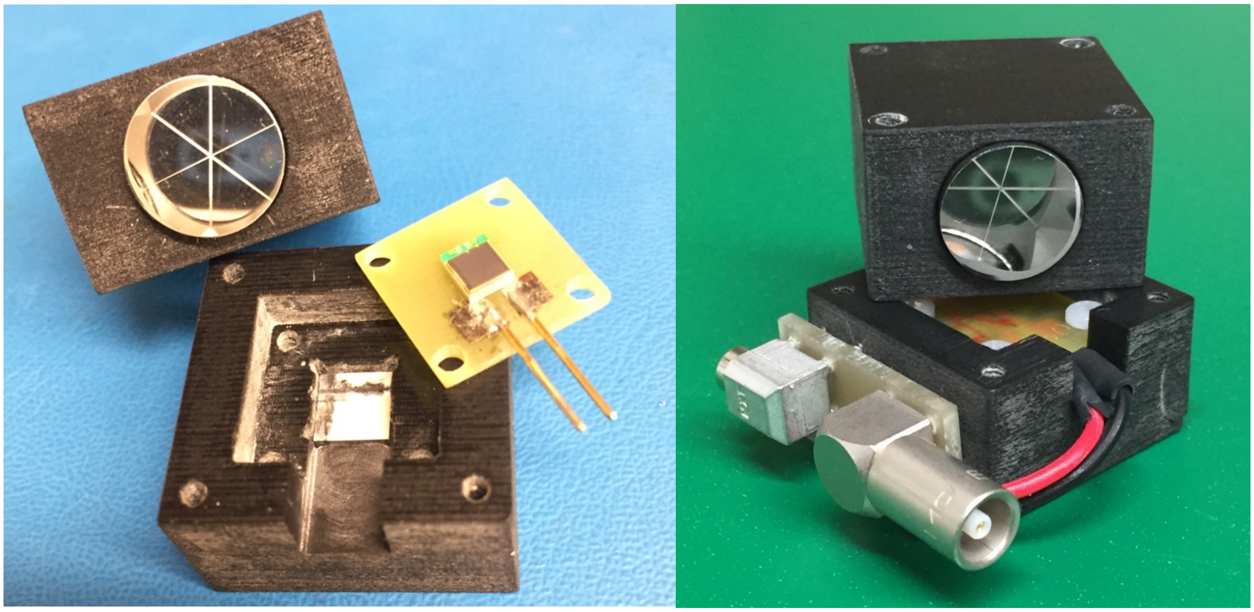

Figure 4.2: The external x-ray detector unit is displayed above. A corner cube is seen embedded in the lid to assist with surveying the location of the device. The output of the detector has connections for both LEMO and mini coax for internal testing and use at PSI. The external edges of the device have been sanded to allow for a smooth surveying surface.

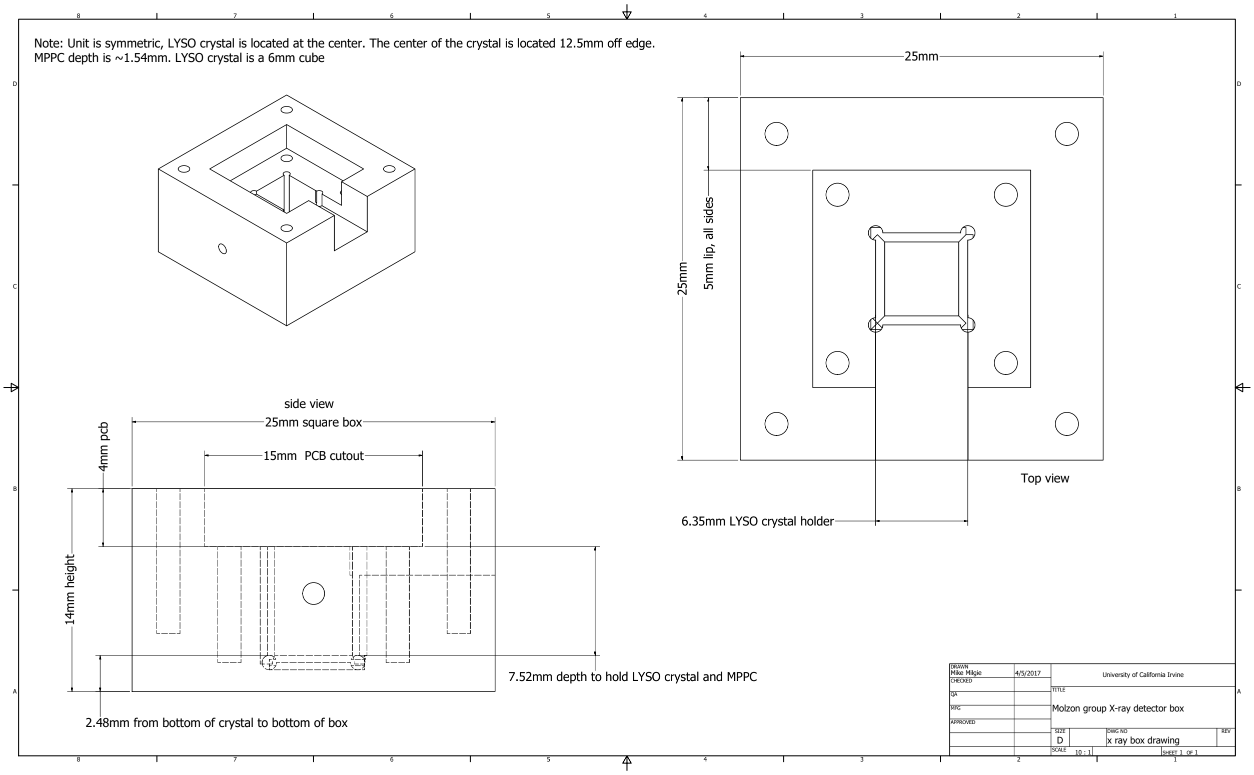

Note: Unit is symmetric, LYSO crystal is located at the center. The center of the crystal is located 12.5mm off edge. MPPC depth is ~1.54mm. LYSO crystal is a 6mm cube

Figure 4.3: The designed specifications of the X-ray detector box are displayed above. The 3mm square MPPC sits at the center of the device on top of the 6mm cubic scintillation crystal.

Figure 4.4 shows the power and amplification system used for our MPPCs. The amplifier is powered by a 12V DC power supply, and the MPPCs need roughly 67V to be powered. To achieve these outputs a 70V Acopian power supply model A70NT25 adjustable power supply is used (seen in yellow), along with a custom PCB (mounted on the yellow power supply of varying voltages) containing Zener diodes and a 12V-70V DC-DC converter. The Zener diodes provide the required 3V drop to provide the MPPC with the required 67V. The PSI amplification system (seen in green) has two inputs; 12V to power the board, and 67V for the detectors [30]. A line out to the detector is connected, the output from the detector is returned to the board, and a final output to the USB DAQ device is connected as the final output. This output is attached to the PSI USB DAQ (small grey box) which is then connected to a computer to read the output. Each MPPC has an optimal powering voltage from 67.17V to 67.19V. These readouts provide an approximate signal to the DAQ electronics used at PSI.

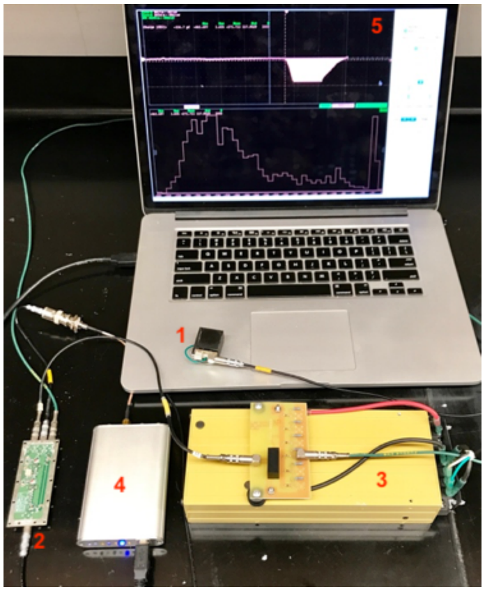

Figure 4.4: The X-ray detector, amplification system, and program used to test the X-ray detectors can be seen above. The X-ray detector in black (1) is connected to the green amplifier PCB on the bottom left (2), which is powered by the yellow power supply (3). The signal is then returned to the grey PSI DAQ (4) and connected to our digital oscilloscope software (5), which can be seen on the laptop.

To read the output from the X-ray detector and amplification system we use a PSI DRS Oscilloscope [30]. As per the Hamamatsu MPPC instructions the software looked for a downward slope trigger. The timing was set to 20ns/division, and the voltage was set to 200mv/division. The delay was adjusted until a clear curve was seen. To measure the signal, the gated charge feature was used, and the integration range was set over the entire curve. The typical settings for detection can be seen below in Figure 4.5.

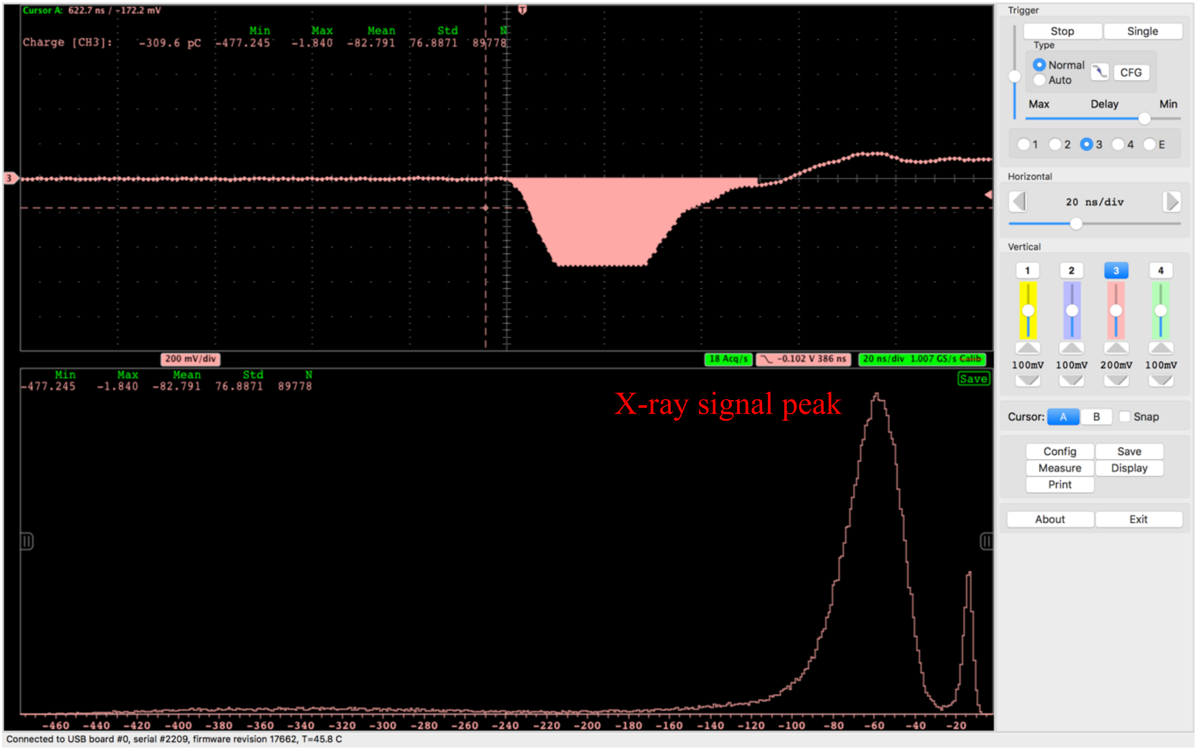

```
Cursor A:  622.7 ns / -172.2 mV
                                 Min       Max      Mean      Std      N
Charge [CH3]:    -309.6 pC  -477.245    -1.840   -82.791   76.8871   89778

200 mV/div        18 Acq/s    -0.102 V 386 ns    20 ns/div  1.007 GS/s Calib

   Min       Max      Mean      Std      N
-477.245    -1.840   -82.791   76.8871   89778

Connected to USB board #0, serial #2209, firmware revision 17662, T=45.8 C
```

Figure 4.5: Typical detection settings can be seen above. The gated charge cursers mark the edges of the characteristic signal detection of the MPPC. The signal is pinned at -0.5V due to a limitation on the DAQ. The signal above with a peak near -60 is characteristic of a hot radioactive source on the target with a LYSO crystal as a scintillator. A histogram feature is implemented to present a characteristic signal detection.

Data was collected for 3 different scintillation crystals, each has a characteristic signal detection and background noise. In the histogram scale seen above the range goes from 0 to -460, these values correlate to the integrated area under the curve in the detected signal. A greater magnitude correlates to a larger energy detected. In the above Figure 4.5 the radioactive Co was placed near the detector, on the order of a few inches away, and the signal was detected. We note the characteristic signal for LYSO scintillators is found with a peak near -60. Noise from background radiation or potential light leaks are seen below in Figure 4.6.

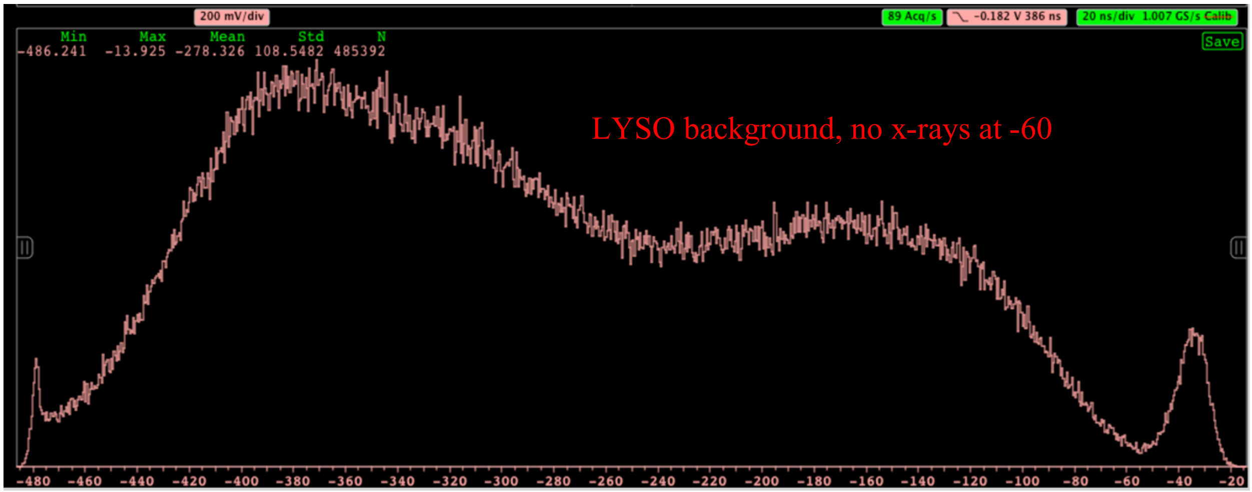

Figure 4.6: Characteristic background noise can be seen above. This noise comes from intrinsic background radiation found in LYSO crystals. We note that in the background noise a clear trend is found, in that no signal is detected at -60. This is ideal for the experimental setup, as the characteristic signal of radioactive Co is found at a value of -60. To insure this effect was due to intrinsic radiation of the LYSO crystal, the detector was placed in a lead pig for 2 hours to create the background noise seen above.

From figures 4.5 and 4.6 it is clear that LYSO scintillators work well to achieve our goal. A clear signal is detectable at -60 when a radioactive Co source is near the detector, and when the source is gone, we get separate background noise, that is absent in the detection region. This characteristic signal detection was found to be consistent in all 4 LYSO crystal scintillators used. However, as can be seen in the following figures, BGO crystals did not share this trend. BGO crystals have a background radiation in the same region as the Co source. This caused background and signal to be indistinguishable, and thus BGO crystals could not be used for the detectors.

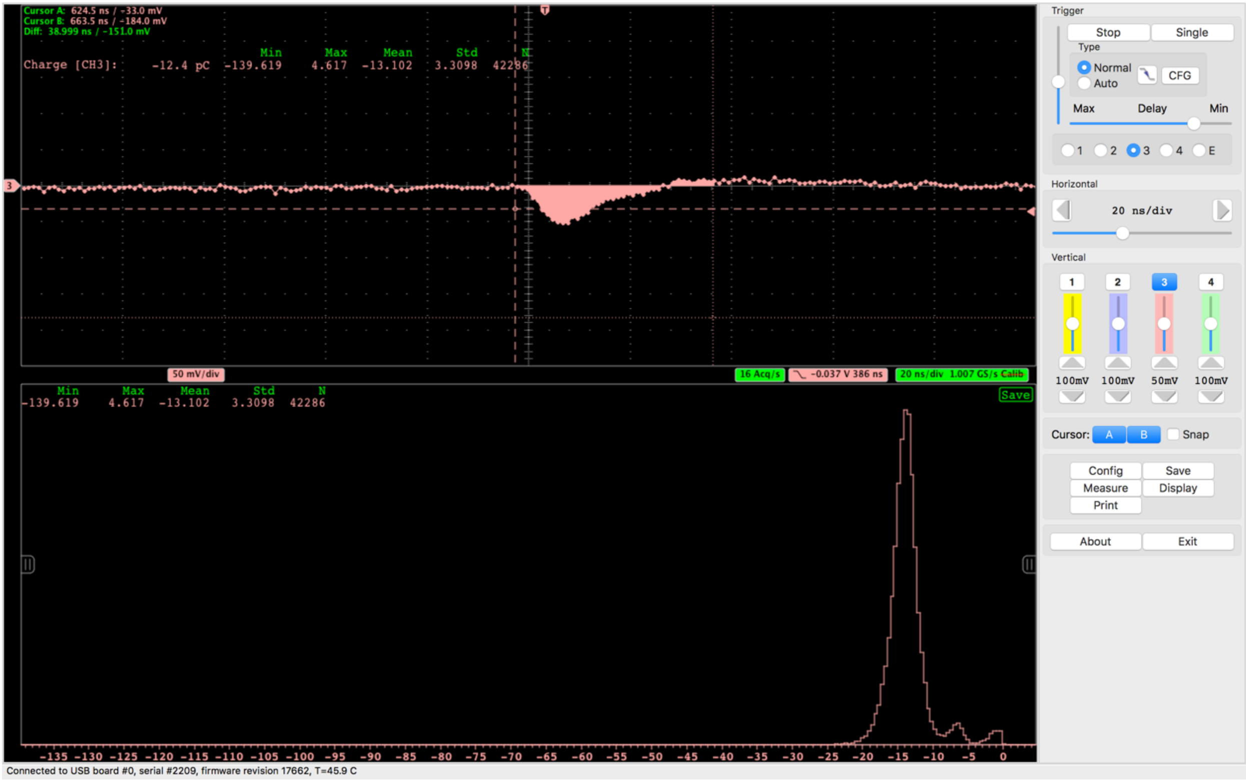

```
Cursor A:  624.5 ns / -33.0 mV
Cursor B:  663.5 ns / -184.0 mV
Diff:  38.999 ns / -151.0 mV
                               Min        Max      Mean       Std       N
Charge [CH3]:     -12.4 pC  -139.619    4.617   -13.102   3.3098   42286
```

```
Min        Max      Mean       Std       N
-139.619   4.617    -13.102    3.3098    42286
```

```
50 mV/div
16 Acq/s    -0.037 V 386 ns    20 ns/div  1.007 GS/s Calib
Horizontal: 20 ns/div
Vertical: 1 100mV   2 100mV   3 50mV   4 100mV
Connected to USB board #0, serial #2209, firmware revision 17662, T=45.9 C
```

Figure 4.7: Characteristic background noise from a BGO crystal can be seen above. We note the background is detected on the histogram with a peak value of -15. This background has a characteristic rate of roughly 15Hz.

As can be seen above in Figure 4.7 the characteristic background signal is found at a histogram value of -15. The characteristic signal detection for BGO crystals is displayed below in Figure 4.8. From these two trials it is clear that both the signal, and background noise, share the same energy on the histogram. We note the acquisition rate is different as expected for the two trials, however since they share the same energy, BGO crystals were found to be unsuitable for X-ray detection.

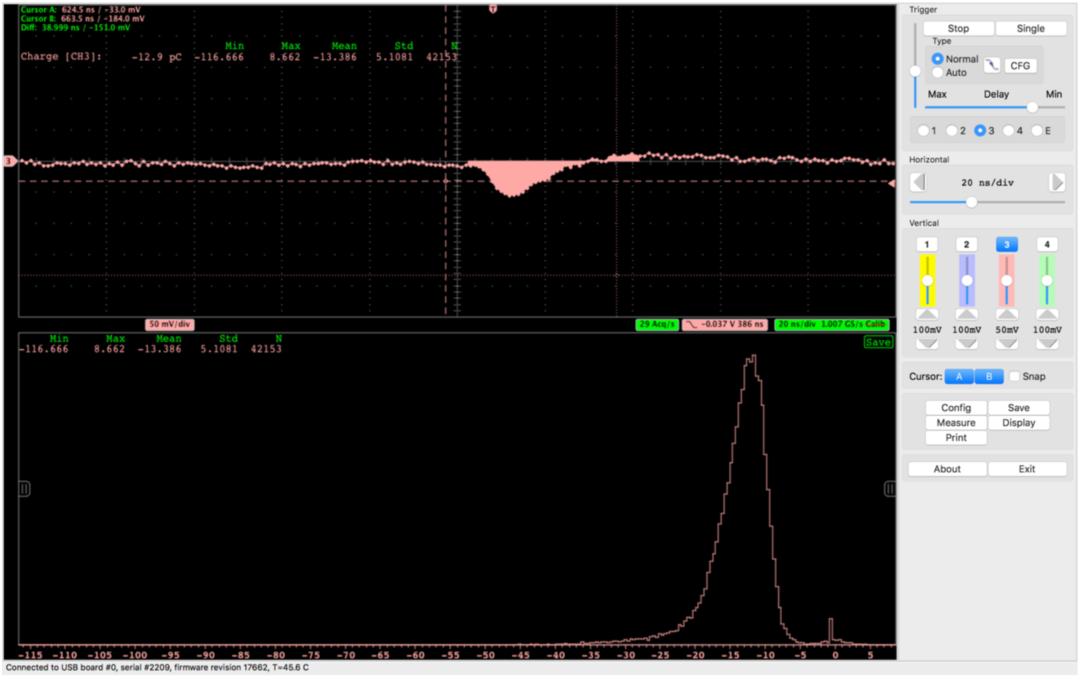

```
Cursor A:  624.5 ns / -33.0 mV
Cursor B:  663.5 ns / -184.0 mV
Diff:  38.999 ns / -151.0 mV
                                    Min       Max      Mean       Std      N
Charge [CH3]:       -12.9 pC  -116.666     8.662   -13.386    5.1081  42153
```

```
   Min        Max      Mean       Std      N
-116.666     8.662   -13.386    5.1081   42153
```

```
Connected to USB board #0, serial #2209, firmware revision 17662, T=45.6 C
```

Figure 4.8**:** Characteristic signal detection for radioactive Co is seen above. Since the signal detection and background noise were found to have the same energy, BGO crystals were determined to be unsuitable for signal detectors.

To determine the effect of light leaking into the detectors a test was completed with no scintillation crystal in the detector box. The MPPC without a crystal has its' own characteristic background noise seen below in figure 4.9. With no scintillator in place no signal is expected. Due to the allowance of some background light we found a slight signal in the low energy range. To nullify any possible light leak, the detectors were sealed with black RTV, however it is clear that light leakage has no effect on the background intrinsic radiation, nor the clear signal detection curves.

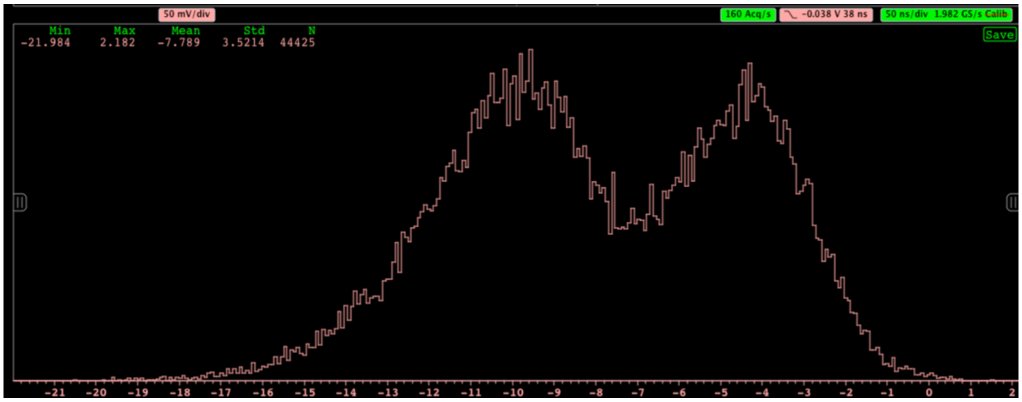

```
  Min      Max     Mean     Std     N
-21.984   2.182  -7.789  3.5214  44425
```

Figure 4.9: A test for the effect of light leakage on the detectors is seen above. It is clear that ambient visible light is out of the range of the characteristic detection and background signals.

The addition of a layer of clear silicon optics grease at the interface between the scintillation crystal and MPPC detector had a clear effect on increasing the signal detection. At this interface, a small gap of air changes the reflective indices and can cause internal refraction of the visible light. By adding a thin layer of optics grease, more signal was found to be transmitted as can be seen below.

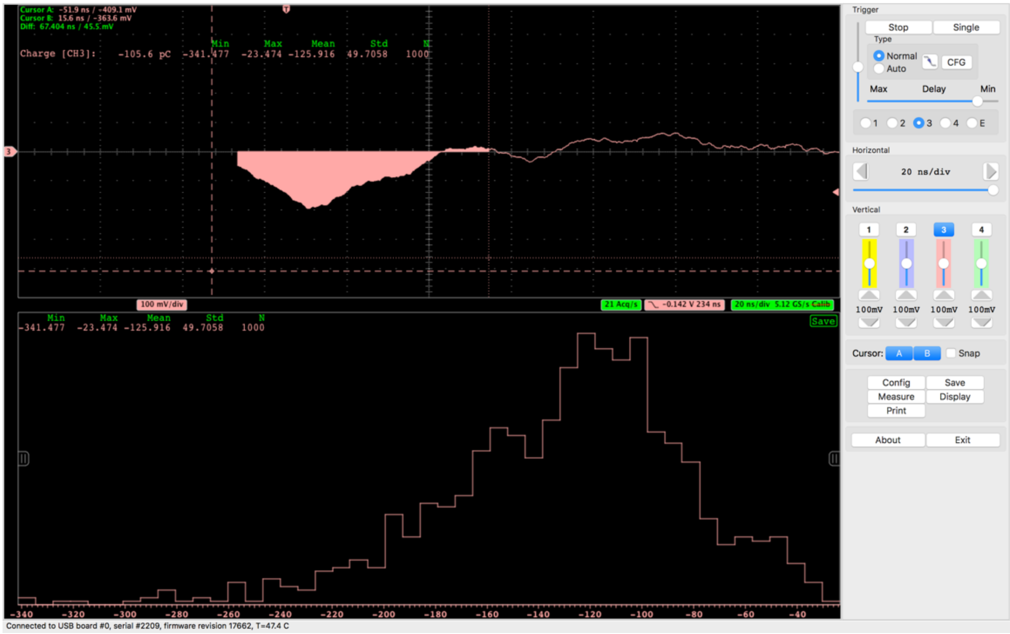

```
Cursor A:  -51.9 ns / -409.1 mV
Cursor B:  15.6 ns / -363.6 mV
Diff:  67.404 ns / 45.5 mV
                                  Min       Max      Mean      Std      N
Charge [CH3]:    -105.6 pC   -341.477   -23.474  -125.916  49.7058   1000
```

```
   Min       Max      Mean      Std      N
-341.477   -23.474  -125.916  49.7058   1000
```

```
Connected to USB board #0, serial #2209, firmware revision 17662, T=47.4 C
```

Figure 4.10**:** Without the use of optics grease, under the same configuration and settings we note a background signal of roughly 200mv is detected. We further note the acquisition rate without optics grease was found to be around 21 Acq/second.

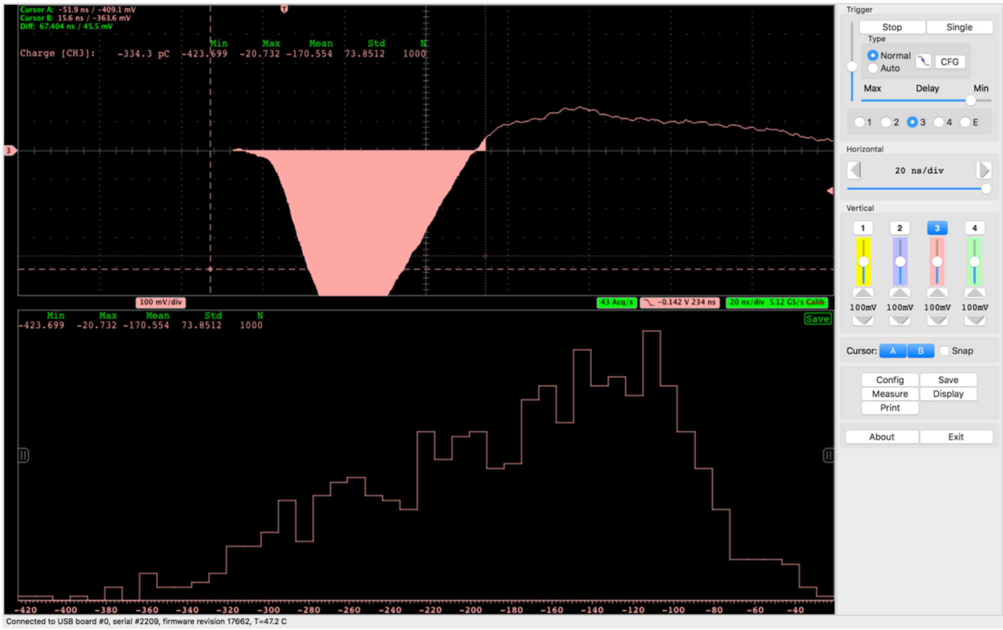

```
Cursor A:  -51.9 ns / -409.1 mV
Cursor B:  15.6 ns / -363.6 mV
Diff:  67.404 ns / 45.5 mV

                                Min       Max      Mean      Std      N
Charge [CH3]:    -334.3 pC  -423.699   -20.732  -170.554  73.8512   1000
```

```
   Min       Max      Mean      Std      N
-423.699   -20.732 -170.554  73.8512   1000
```

Connected to USB board #0, serial #2209, firmware revision 17662, T=47.2 C

Figure 4.11**:** By adding optical grease it can be seen the signal amplitude increases to the peak value of 500mv, and the acquisition rate is also increased two fold.

Thus far LYSO scintillators have proven to be effective at signal detection and BGO crystals have been shown to have the same signal and background detection energy, thus proving them unusable for our purposes. Two separate types of LYSO crystals have been tested and are being used at PSI. One is the standard LYSO crystal, of which the results have already been presented. The second type of LYSO crystal used has a reflective coating on 5 of the 6 sides of the crystal, with the one uncoated side facing the MPPC detector. The effect of the reflective coating allows more light to hit the MPPC, as instead of scattering out the edges of the crystal and being absorbed by the black PLA plastic box, the light is reflected and absorbed by the MPPC. While both the standard and coated LYSO crystals have the same characteristic signal detection energy, the characteristic background noise differs. Characteristic LYSO background noise is seen above in Figure 4.6 and can be compared to the background noise of coated LYSO crystals seen below in Figure 4.12.

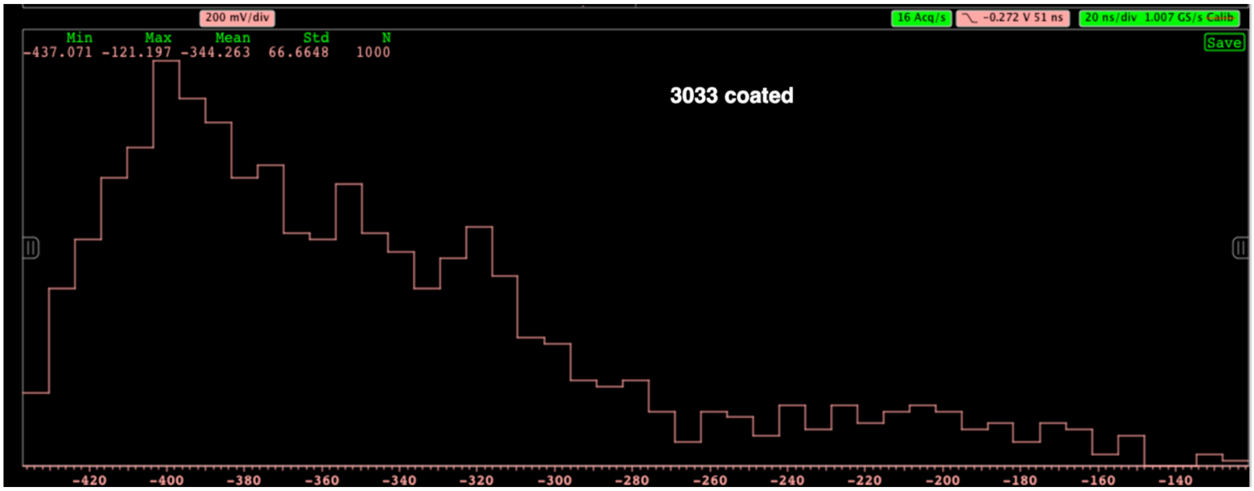

```
  Min      Max      Mean      Std      N
-437.071 -121.197 -344.263  66.6648   1000
```

Figure 4.12**:** As can be seen above, a coated LYSO crystal has in general, a higher characteristic background energy. This allows the crystal to be useful in detection, as the background noise is nowhere near the characteristic signal detection of -60.

The detectors can be used with our collimators to test spot size and shape. Details of the specifications of our collimator are given in appendix D. For the first test, our Co-57 source was placed in a lead collimator with the active end pointing towards the detector. The collimator was mounted on the rotational stage of our translational table, and the source was moved a total of 10 cm with data taken over 16 degrees at each Z location. The detector was placed roughly 30cm from the source. At each point four acquisition rates were measured, an average was taken, and the result is seen below in table 4.1. As the source gets near the center of the detector we see our acquisition rate go from background of ~20 acq/second, to the max value of ~600 acq/sec. The results from this experiment clearly show the lead collimator has a round spot size. The signal for the lead collimator can be clearly detected over a distance of 6cm, and a range of 11 degrees in phi rotation.

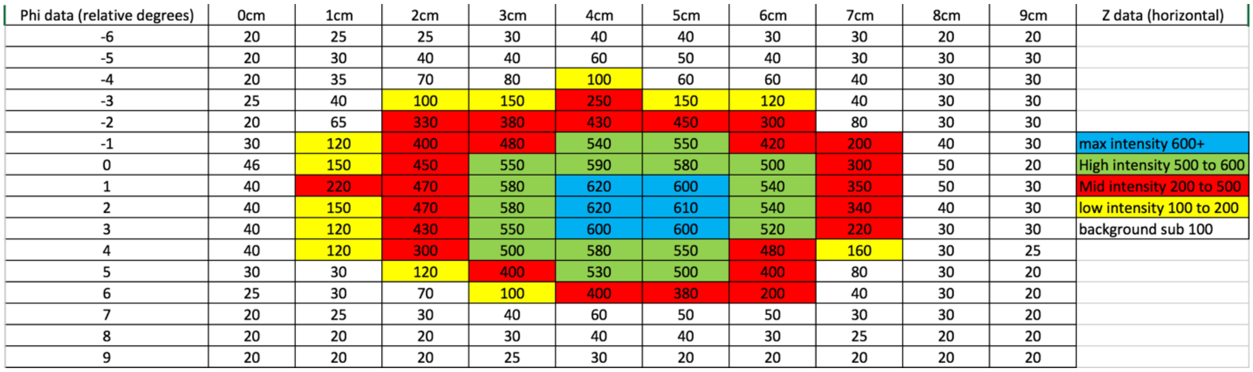

Phi data (relative degrees)	0cm	1cm	2cm	3cm	4cm	5cm	6cm	7cm	8cm	9cm	Z data (horizontal)
-6	20	25	25	30	40	40	30	30	20	20	
-5	20	30	40	40	60	50	40	30	30	30	
-4	20	35	70	80	100	60	60	40	30	30	
-3	25	40	100	150	250	150	120	40	30	30	
-2	20	65	330	380	430	450	300	80	30	30	
-1	30	120	400	480	540	550	420	200	40	30	🟦 max intensity 600+
0	46	150	450	550	590	580	500	300	50	20	🟩 High intensity 500 to 600
1	40	220	470	580	620	600	540	350	50	30	🟥 Mid intensity 200 to 500
2	40	150	470	580	620	610	540	340	40	30	🟨 low intensity 100 to 200
3	40	120	430	550	600	600	520	220	30	30	background sub 100
4	40	120	300	500	580	550	480	160	30	25	
5	30	30	120	400	530	500	400	80	30	20	
6	25	30	70	100	400	380	200	40	30	20	
7	20	25	30	40	60	50	50	30	30	20	
8	20	20	20	30	40	40	30	25	20	20	
9	20	20	20	25	30	20	20	20	20	20	

Table 4.1**:** The intensity of the Lead collimator with a hot source can be seen above. The max acquisition rate of the detector was found to be ~600 acq/sec, with background noise around 20 acq/sec. The shape demonstrates we indeed have a round collimator as expected, and further characterizes a direct detection with the maximum intensity.

Radioactive materials are known to follow the inverse square law with the intensity I, being proportional to the inverse of the distance D squared. Thus it is expected the intensity should follow the formula: I ~ $\frac{1}{D^2}$. The results found when testing the intensity detected, measured in acquisitions per second vs distance are displayed below in Figure 4.13. The radioactive source itself is contained in a small metal container, with the source closer to one end, and more attenuated on the other end. Thus one side of the source is much stronger than the other side. For the purpose of this paper the more radioactive end is called the "Business end". The lead collimator, much more narrow brass collimator, and the source without a collimator were all tested at various distances to test the sensitivity of our X-ray detectors. The results show that our detectors are extremely sensitive, and can detect a signal at a far greater distance than is required for the experiment at PSI.

This oversensitivity is useful and acceptable with a proper DAQ, however the DAQ we used for these trials is USB 2.0, and was thus limited by the data transfer rate. This limitation pinned the output to a max of ~660 acq/second, and so the characteristic inverse square law output is not fully seen for all tests performed. Nonetheless it is clear a signal can be detected from both collimators as well as the source without a collimator. A signal was able to be detected at 2.5 meters with the source. At PSI the maximum detection distance required is on the order of 60cm. A new, stronger source was also purchased with a radioactivity nearly 30 times stronger than the one tested here.

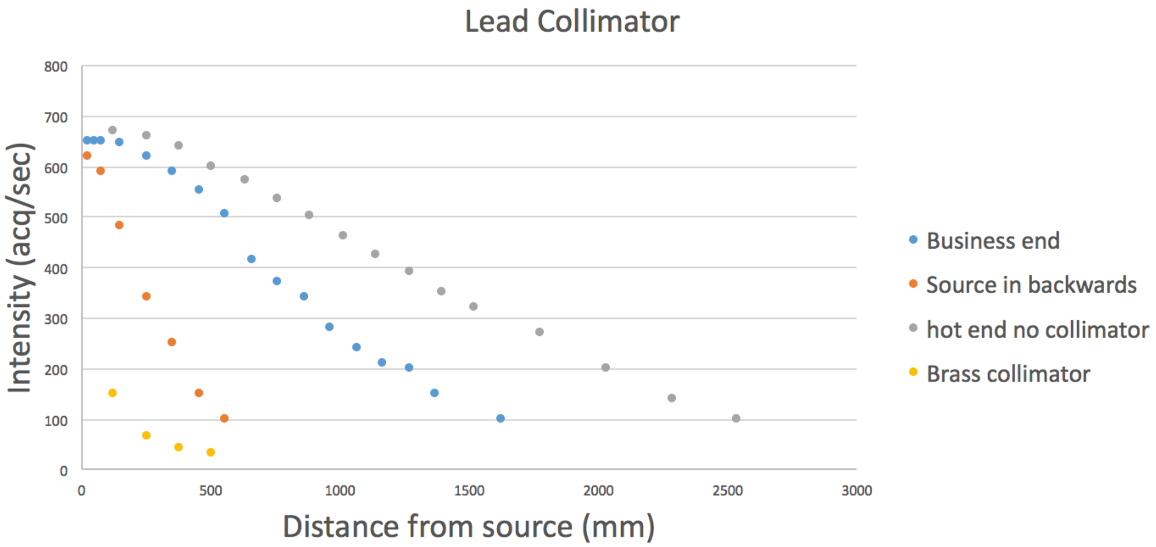

Figure 4.13: The intensity of the lead collimator can be seen above in blue and orange, and is compared with a much smaller brass collimator in yellow, and the source without a collimator in grey. As can be seen, the DAQ used was limited by the USB 2.0 interface and so intensity greater than ~600 acq/sec is pinned. When the source is attenuated by placing it in the collimator backwards (orange) it is clear we see the $1/D^2$ trend, along with in the brass collimator, where the small hole size greatly attenuates the signal. The detector is seen to be very sensitive, with detection as far away as 2.5 meters using a ~7mCi source.

To conclude, we have shown how our X-ray detectors work, how background data is distinguished from a radioactive source detection, the sensitivity of the devices, as well as results from testing the device with various collimators. It has been shown that LYSO scintillators work well with our 122kEv signal, whereas BGO crystals have proven ineffective. The use of optical grease has been shown to increase signal sensitivity. We have further presented the round shape of our lead collimator, and performed testing at various distances to verify the detectors will be of use in crosschecking the position of internal MPPCs at the MEGII experiment in PSI. These 6 devices will be placed on the exterior of the cryostat, and with optical survey of the boxes can be used to crosscheck a location on the outside of the cryostat with a signal detection inside of the liquid xenon tank.

Chapter 5: Experimental Results and Conclusion

Our novel alignment system was shipped to the Paul Scherrer Institut in April of 2017 and successfully installed in the MEG II experiment. The device was properly aligned and produced characteristic motions detected by the photodector system. An optical survey was performed on the collimator as it translated the full Z distance to monitor and confirm any deviations detected by the photodetector. The optical survey results demonstrated the system was aligned properly, and had a constant collimator line in Z to within the precision of the optical survey device of 0.3mm. In June 2017 the alignment device was used to calibrate the 4092 MPPC array to a precision of roughly 0.2mm. Images of the alignment device mounted in the COBRA magnet are shown in Figures 5.1 and 5.2.

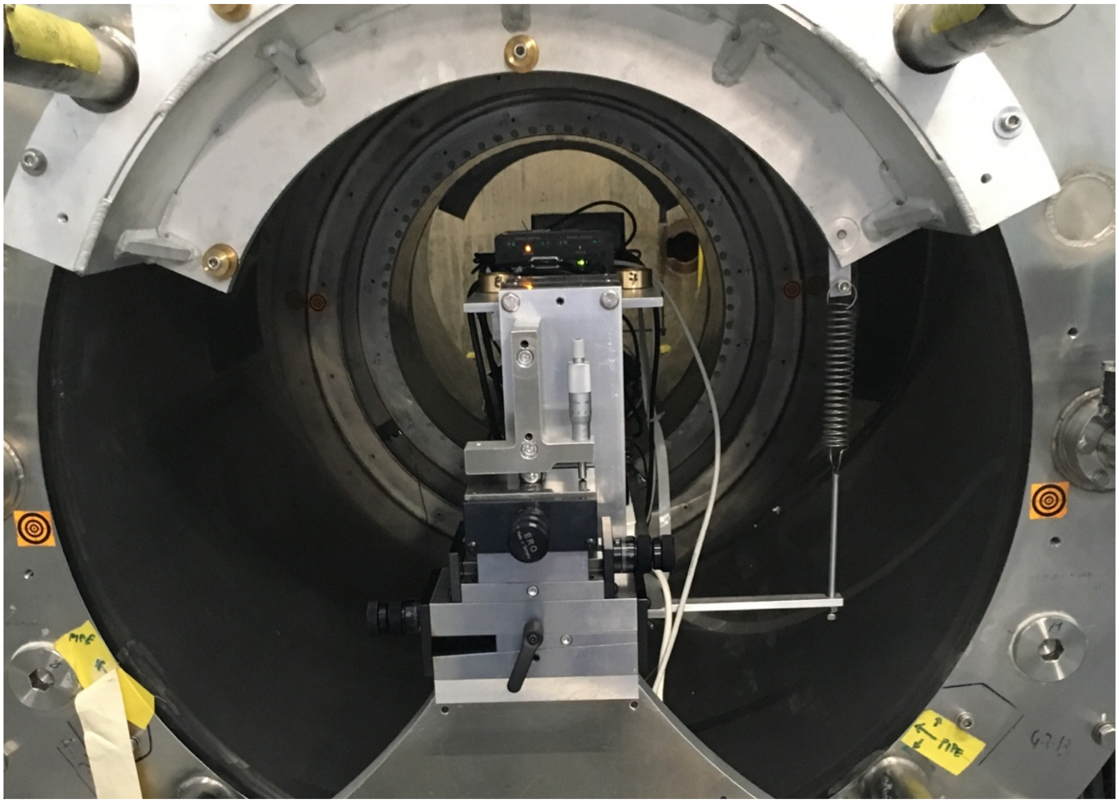

Figure 5.1: Our novel alignment device can be seen mounted in the COBRA above. A spring and fine adjustment system were implemented to control the position of the I beam with respect to the centerline of the MEG II experiment.

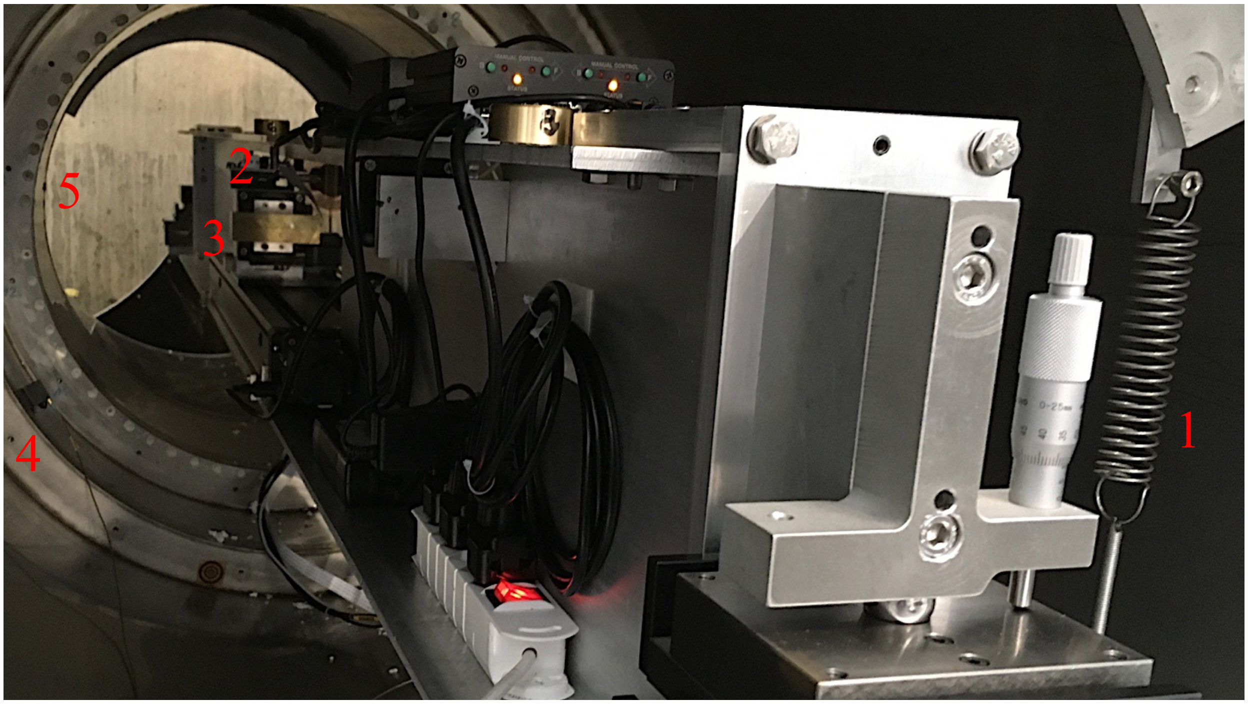

Figure 5.2: A larger image of our alignment device can be seen above. The spring on the right (1) balances the extra weight found on the left side of the alignment system due to the collimator and rotational stage (2). The brass collimator (3) can be seen near the upper left, this points towards the 4092 MPPC array we have calibrated as it translates across the full Z distance of the array, and sweeps over the full phi motion of the LXe. A LYSO X-ray detector (4) can be seen on the far left of the image in black, and was used to crosscheck position. The inner diameter of the magnet can be seen in the upper left (5).

The collimator was first placed in the horizontal direction, such that the X-ray beam hit 3 target MPPCs in the Z direction at one specific phi orientation at a time. The device ran over the entire translation distance to hit all MPPCs and test both their functionality and position. Our alignment device was then removed from the COBRA, and the collimator was rotated 90 degrees. In the new orientation, the collimated beam strikes 3 MPPC targets in the phi direction, and one target in Z. The device was again surveyed using optical survey to determine the precise location of the collimator, and to fine adjust the position of the I beam such that it was positioned in the center of the COBRA. The device was found to successfully strike and calibrate half of the MPPCs near Z=0. At larger ‖ Z ‖ the magnet had thicker coil's and adsorbed the x-rays.

Our X-ray detectors were successfully mounted both on the inside of the COBRA and the outside wall of the COBRA closest to the LXe to crosscheck the external position of the collimator and alignment system. The LYSO X-ray detectors were implemented and successfully used with the WaveDREAM data acquisition system to detect background noise and a clear source signal. The WaveDREAM is a novel device created by PSI with sampling rate of 5Gb/s and allows for a much greater sampling rate than the DRS4 evaluation board [3, 31]. The devices' positions were measured via the aforementioned optical survey process. The results allowed a position crosscheck to a resolution of 0.3mm as expected. The characteristic background and signals are also presented in figures 5.4 and 5.5.

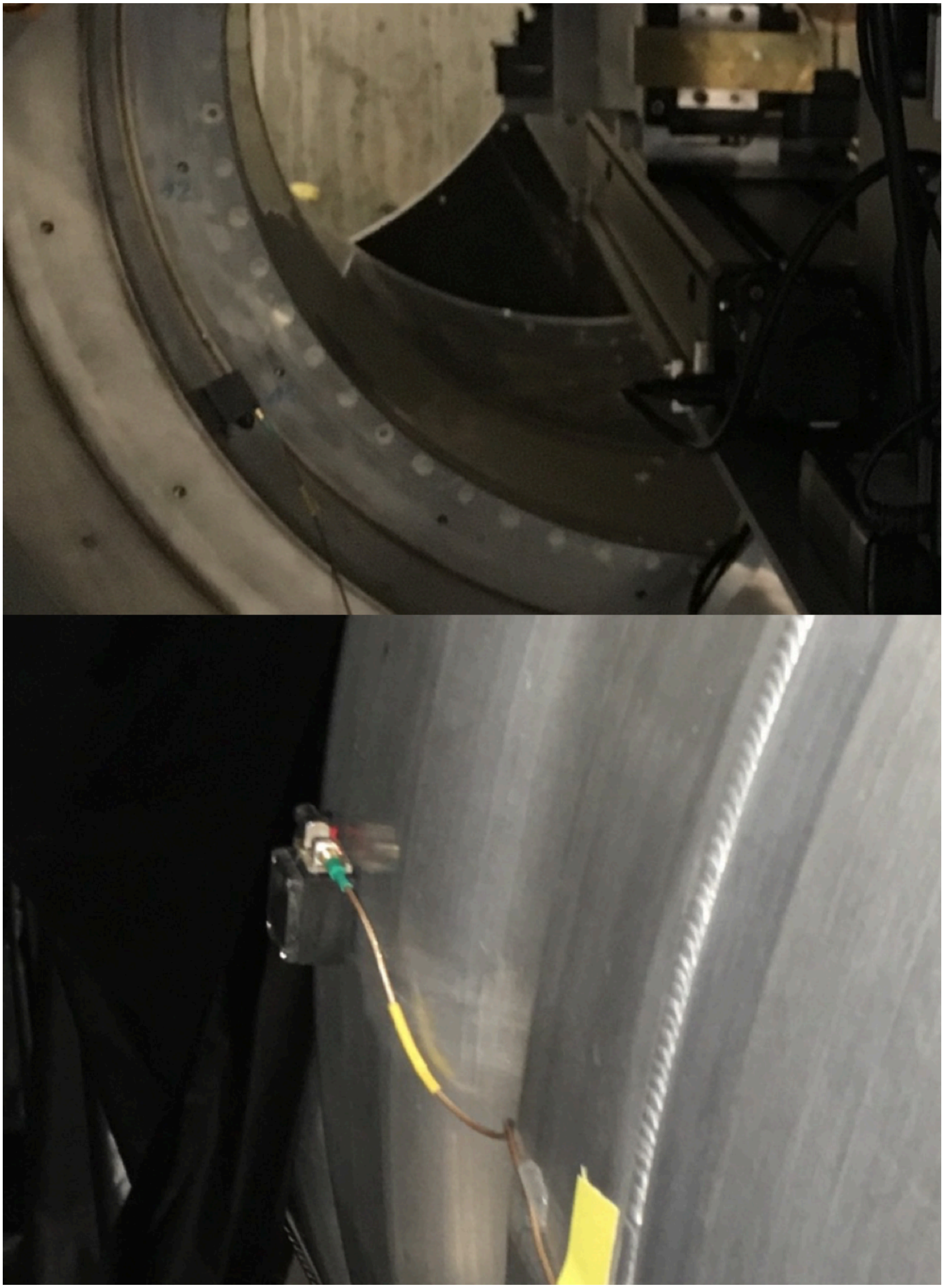

Figure 5.3: Our LYSO X-ray detectors can be seen above on the inside of the COBRA (top) and on the outer wall of the COBRA nearest to the LXe (bottom).

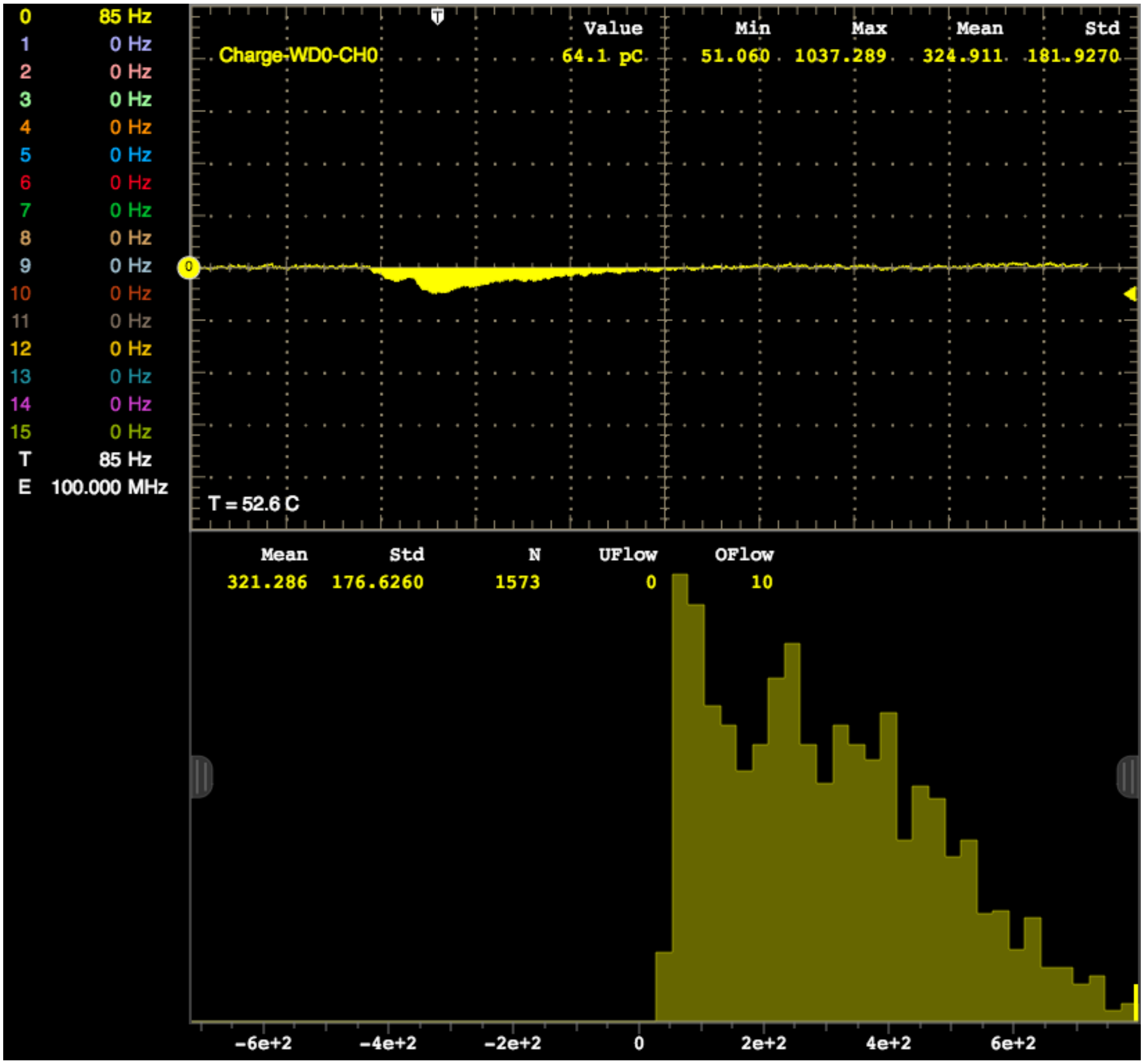

0	85 Hz
1	0 Hz
2	0 Hz
3	0 Hz
4	0 Hz
5	0 Hz
6	0 Hz
7	0 Hz
8	0 Hz
9	0 Hz
10	0 Hz
11	0 Hz
12	0 Hz
13	0 Hz
14	0 Hz
15	0 Hz
T	85 Hz
E	100.000 MHz

	Value	Min	Max	Mean	Std
Charge-WD0-CH0	64.1 pC	51.060	1037.289	324.911	181.9270

T = 52.6 C

Mean	Std	N	UFlow	OFlow
321.286	176.6260	1573	0	10

Figure 5.4: The characteristic background signal of our LYSO X-ray detectors can be seen above using the PSI WaveDREAM Oscilloscope. The background is rather broad due to intrinsic radioactivity of the LYSO scintillator. The device was allowed to collect roughly 1500 background data points before the collimator was moved into position.

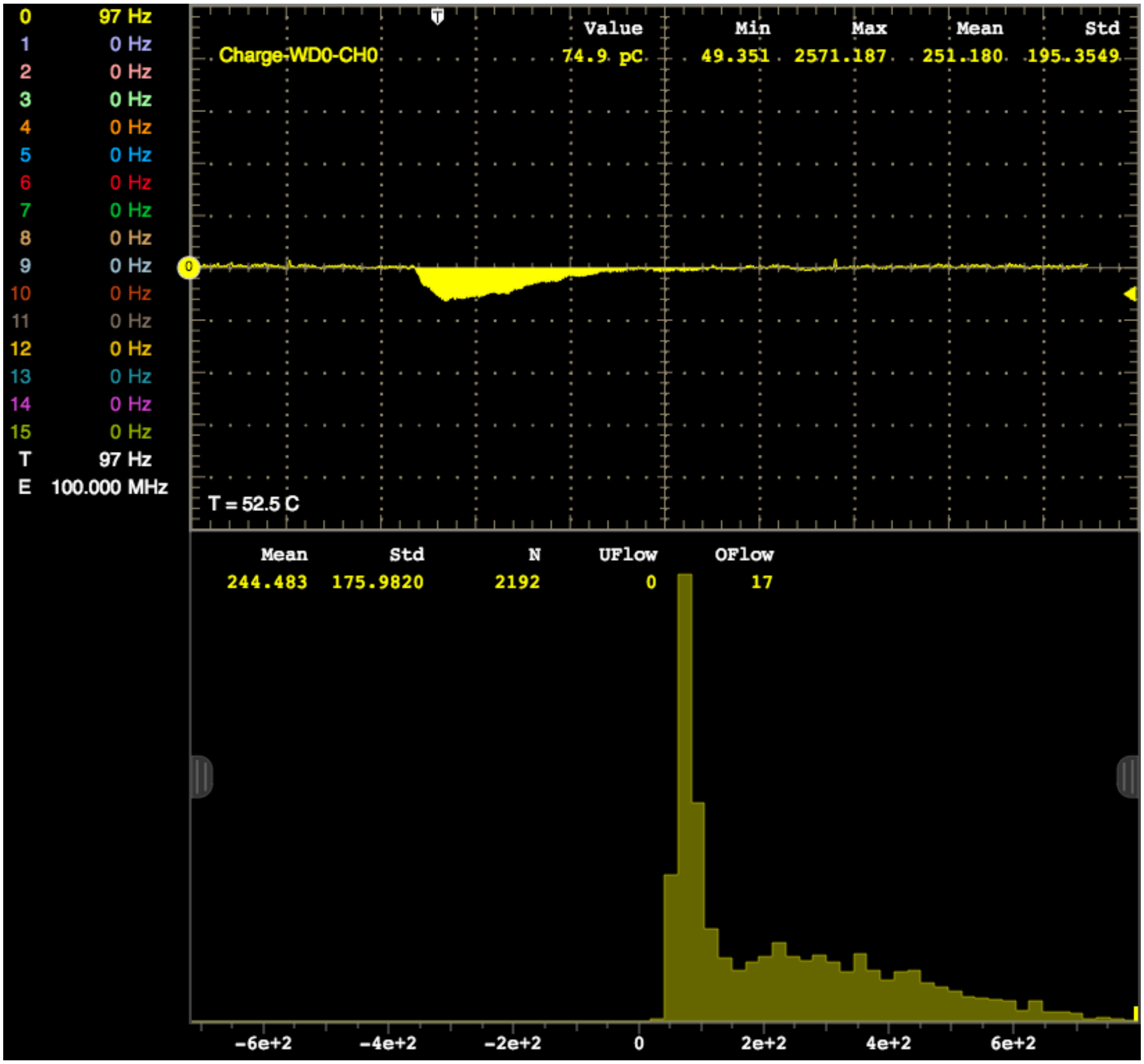

Figure 5.5: After taking ~1500 data points from background signal, the collimator was then translated into the proper position. The detector clearly showed the signal dominates the background noise with ~600 interactions of signal displayed above. This output is the combination of ~1500 background points, along with ~600 signal interactions. The signal can be seen clearly with the largest peak located on the horizontal axis with a value of ~75. These results agree well with our prior results found using the DRS4 evaluation board and described in detail in chapter 4 of this thesis.

A final crosscheck we implemented to align and calibrate the MPPC array was to mount lead attenuation devices to the outer wall of the LXe. The purpose of this lead is to block our radioactive Co-57 signal from the MPPCs found at that specific location. By doing this we allow for an external crosscheck on position, and have a correlation with what is occurring inside the LXe tank. With the lead in place, the X-rays emitted at that location should be absorbed, and thus some of the MPPCs should not receive a signal. Therefore, there should be clear locations were the MPPC does not absorb light from scintillation in the LXe. These lead holders were optically surveyed to provide a position crosscheck between the exterior and interior of the tank. A few of these lead attenuation devices can be seen in the figure below.

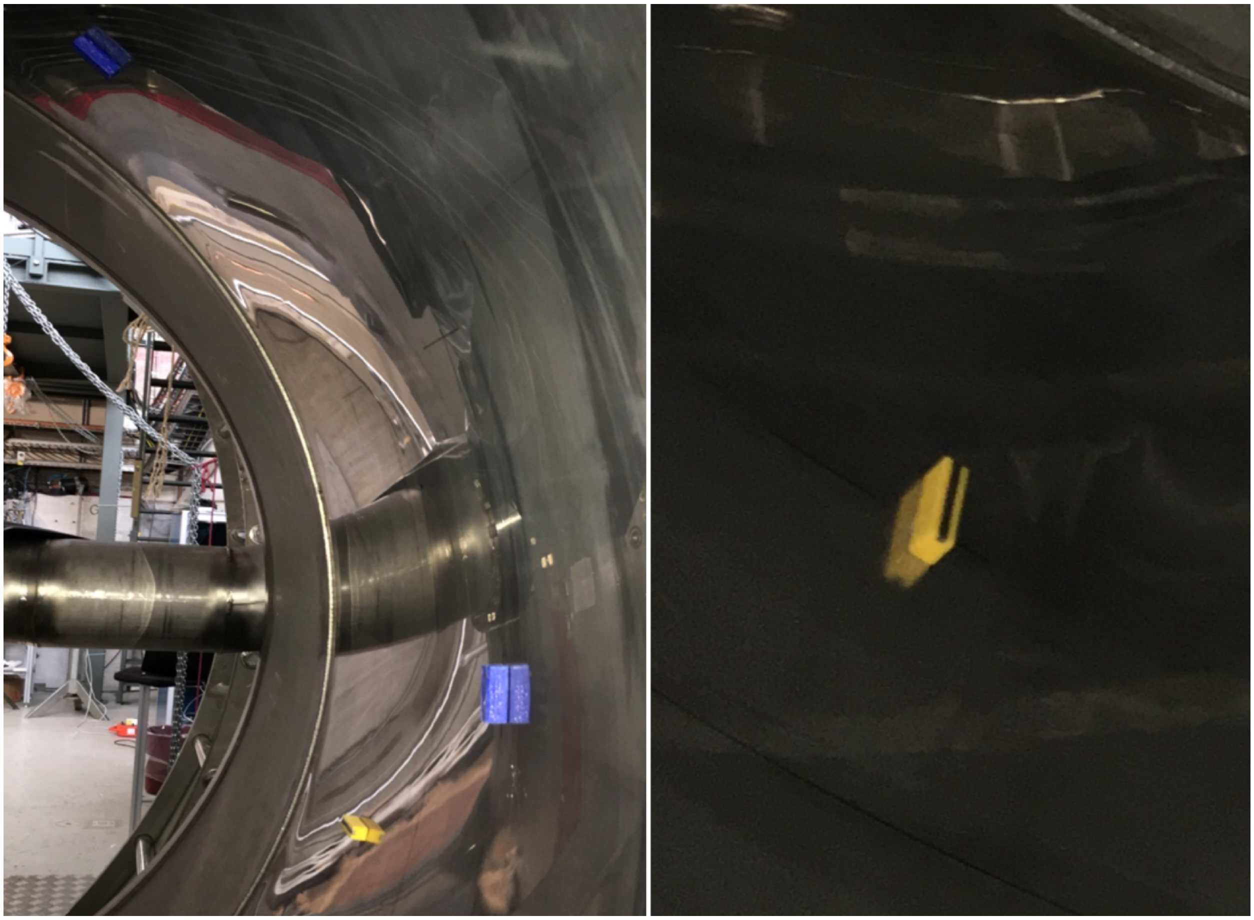

Figure 5.6: Lead attenuation devices can be seen above. They are housed in blue (vertical) and yellow (horizontal) PLA plastic holders, and mounted with double sided tape.

The goal of this project, to align the 4092 MPPC positions in a fully operational configuration was successful. The technique used modest beam time and was shown to be repeatable. Our optical crosscheck system using X-ray detectors and lead attenuators succeeded as a position crosscheck and allowed a direct correlation between the LXe and DC alignment.   The alignment device was capable of outperforming the goal precision of 1mm by a factor of three, and allowed for calibration of 2000 MPPC in the MEG II with a precision of 0.2mm.

Appendix A: Quadrant photodetector calibration

To detect rotations in pitch and yaw of our calibration device a laser and four quadrant OSI optoelectronics silicon photodiode amplifier module was implemented [29]. The detector is located 63cm away from the laser/collimator system at the closest approach, and 137cm away at the point furthest away. The detector is connected to an ADC ADS1115 and the raspberry Pi to read the output from the device; the wiring setup is shown in Appendix C. In this appendix we present the working principle of the photodetector along with the calibration technique and the results.

The four quadrant photodiode module has four separate photodiode elements separated by a small gap on a common substrate and shared cathode. The anode of each element is individually available so that a single quadrant can be electrically characterized [29]. As a laser spot is translated over the detector, the energy is distributed between the four elements to define a position. Since the transfer function for a circular spot is not linear, due to the linear movement not being proportional to the percentage of its area which shifts, an angled beam is used. By using a laser rectangular spot angled at 45 degrees the best linearity is achieved. For centering applications, the segmented photodiodes are unparalleled with resolutions on the order of 0.1 μm [29].

A simple schematic of the photodiode can be seen in figure A.1. The device provides three output values, one is the sum of the total currents to provide an intensity detected, the others are for the vertical and horizontal intensities. These values are calculated by taking the difference between the top and bottom currents, and the left and right currents. The equations governing these outputs are also displayed below.

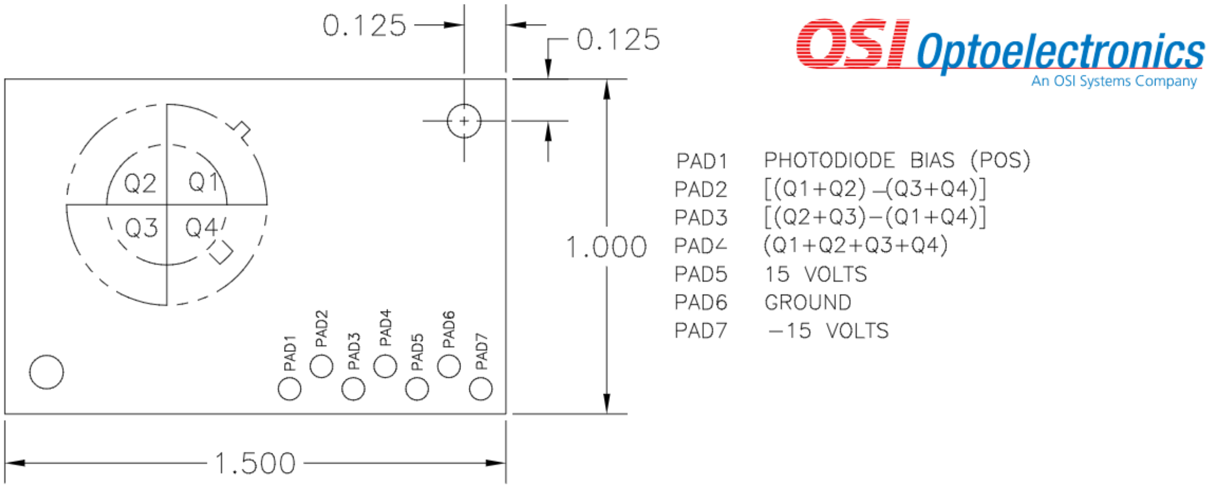

Figure A.1: A simple schematic of the photodetector can be seen above [29]. The device is powered by a +-15V power supply, and the outputs can be found on pads 2, 3, and 4. Typical values for the sum output (Pad 4) were of order ~1000. When the laser is centered pads 2 and 3 produce an output of ~0.

$$V_{T-B} = -\lfloor (i_1 + i_2) - (i_3 + i_{4)}) \rfloor \times 10^4$$

$$V_{L-R} = -\lfloor (i_2 + i_3) - (i_1 + i_{4)}) \rfloor \times 10^4$$

$$V_{SUM} = -(i_1 + i_2 + i_3 + i_4) \times 10^4$$

The equations governing the output of the detector can be seen above. $V_{T\text{-}B}$ produces the vertical output, while $V_{L\text{-}R}$ provides the horizontal output. V_{Sum} produces the total intensity detected. To normalize our data, the outputs $V_{T\text{-}B}$ and $V_{L\text{-}R}$ were divided by V_{Sum} [29].

The arithmetic position of the spot is therefore characterized as seen below [29].

$$X = \alpha \frac{(i_2 + i_3) - (i_1 + i_4)}{i_1 + i_2 + i_3 + i_4}$$

$$Y = \beta \frac{(i_1 + i_2) - (i_3 + i_4)}{i_1 + i_2 + i_3 + i_4}$$

With the output and arithmetic of the photodetector known, a calibration must be performed to determine how the variance in X and Y correlate to a distance in mm, and ultimately the angle of pitch and yaw induced. The photodector was mounted in a box attached to a translational unit capable of translating the detector in the X and Y directions. These translations are controlled by two adjustment screws with a known displacement of 0.25mm/turn. Thus by translating the box/photodetector a known distance, and measuring the change in X and Y positions, a calibration curve could be created. In the following we present the technique used to characterize and verify the calibration of the device to acquire the pitch and yaw of the system.

The detector box was translated such that the laser was on the left edge of the detector and output the maximum value in the horizontal direction of ~+1000. The box was then rotated one full turn (0.25mm) so that the laser moved closer to the right edge of the detector (where a value of ~-1000 is output). For a reference of the output values of the detector refer to Figure 3.1. The full dataset from this test can be seen in the table and graphs below. It can be noted that vertical intensity does vary a bit over the entire translation, however it is minimal and of order ~0.1mm. We further note the total intensity has a variance of roughly 4%, this effect is most likely due to minor perturbations in the polarizing lens placement or slight angle of the laser with respect to the detector location. To protect the detector itself, a polarized lens was placed in front of the detector to minimize background noise from ambient lights, any debris, or an overly strong laser.

Vertical Int	Horizontal Int	Total Int	Horiz Int/Total int	Dist in mm from center
-92	1026	1057	0.9707	1.875
-77	975	1053	0.9259	1.625
-66	891	1047	0.8510	1.375
-55	774	1042	0.7428	1.125
-48	630	1037	0.6075	0.875
-41	464	1034	0.4487	0.625
-45	282	1031	0.2735	0.375
-52	82	1030	0.0796	0.125
-70	-127	1026	-0.1237	-0.125
-80	-350	1023	-0.3421	-0.375
-97	-585	1018	-0.5746	-0.625
-80	-806	1028	-0.7840	-0.875
-52	-952	1050	-0.9067	-1.125
-24	-1015	1062	-0.9557	-1.375

Table A.1: A typical output from the photodetector is displayed above as the laser is swept across the horizontal axis while aligned near the vertical center of the detector.

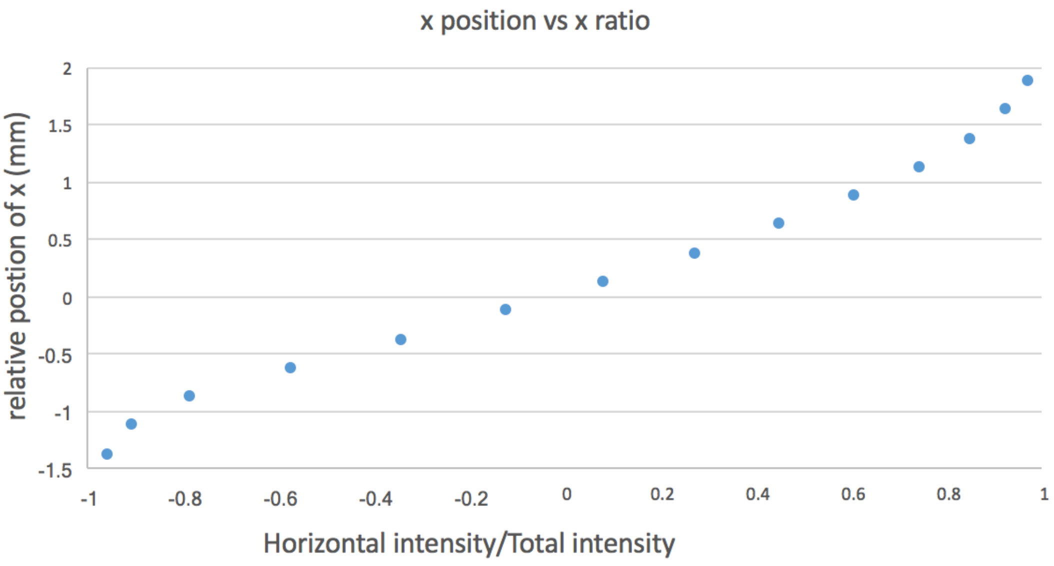

Figure A.2: A plot of a horizontal sweep is displayed above. We note near the edges we see a non-linear effect. This is expected due to the spot size and shape of the laser. As the laser translates off target, the detector can no longer produce an accurate output of position. Thus to calibrate the device, the edges are neglected, as during normal use the alignment system uses only the central, linear region of the photodetector.

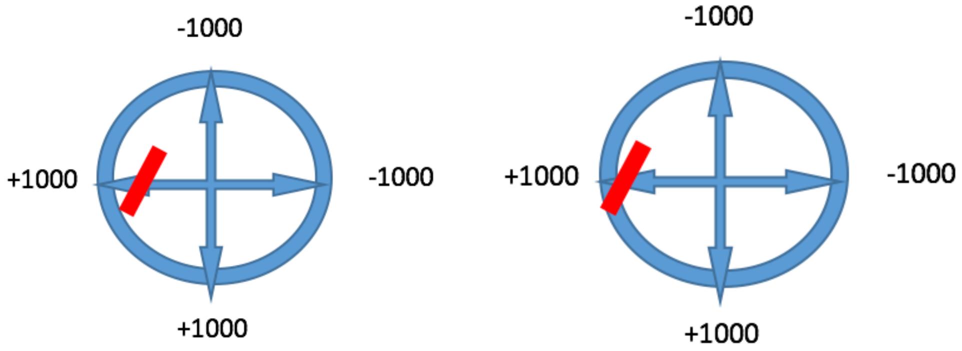

Figure A.3: As the laser translates near the edges of the detector, it begins to move off the detection region seen on the right. This effect causes the position of the detector to be moved, however the output of the detector remains near constant. Thus the region near the edges produces a non-linear trend seen in the plots above. Data from this region is neglected.

Position (mm)	Vertical	Horizontal	Intensity	vert/Int	Horiz/Int
0	-8	-8	1016	0.0079	0.0079
0.25	219	222	1024	0.2139	0.2168
0.5	430	435	1032	0.4167	0.4215
0.75	618	620	1044	0.5919	0.5938
1	786	791	1051	0.7479	0.7526

Table A.2: The table above describes the output when both horizontal and vertical directions are shifted by one full rotation of the translation stage mounted to the quadrant photodetector. The output demonstrates that the horizontal and vertical output intensities are near identical when shifted the same amount and show variance of less than 1%. This result supports our hypothesis that both horizontal and vertical should have nearly the same calibration slope.

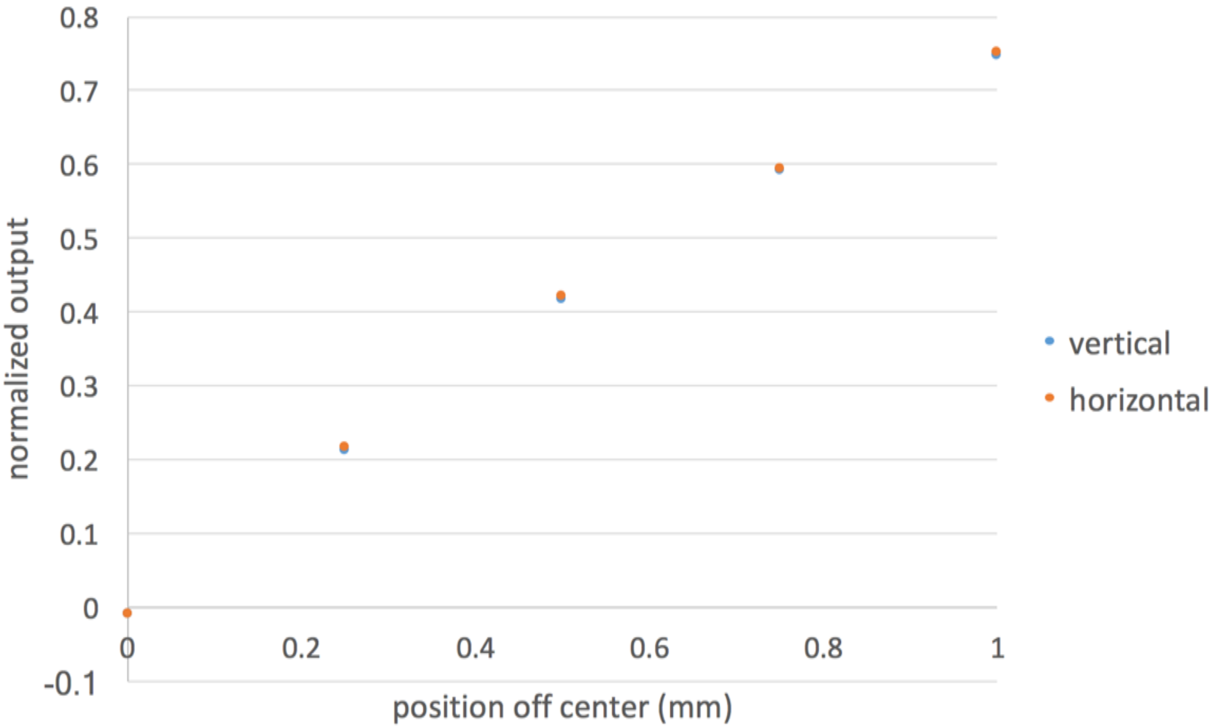

Figure A.4: The above plot demonstrates that both vertical and horizontal share near the same slope and should have a calibration curve within 1% of each other. The blue data points are difficult to see because they are so close to the horizontal data points.

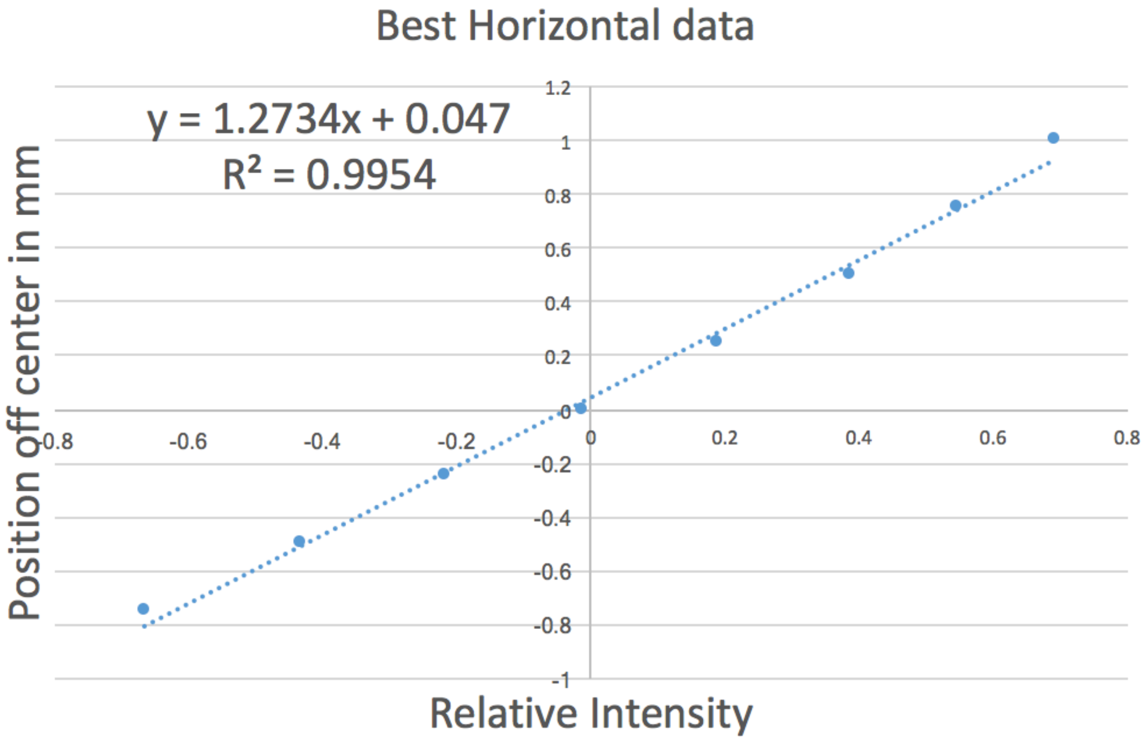

Figure A.5: The final calibration curve for the horizontal QPD fit is displayed above.

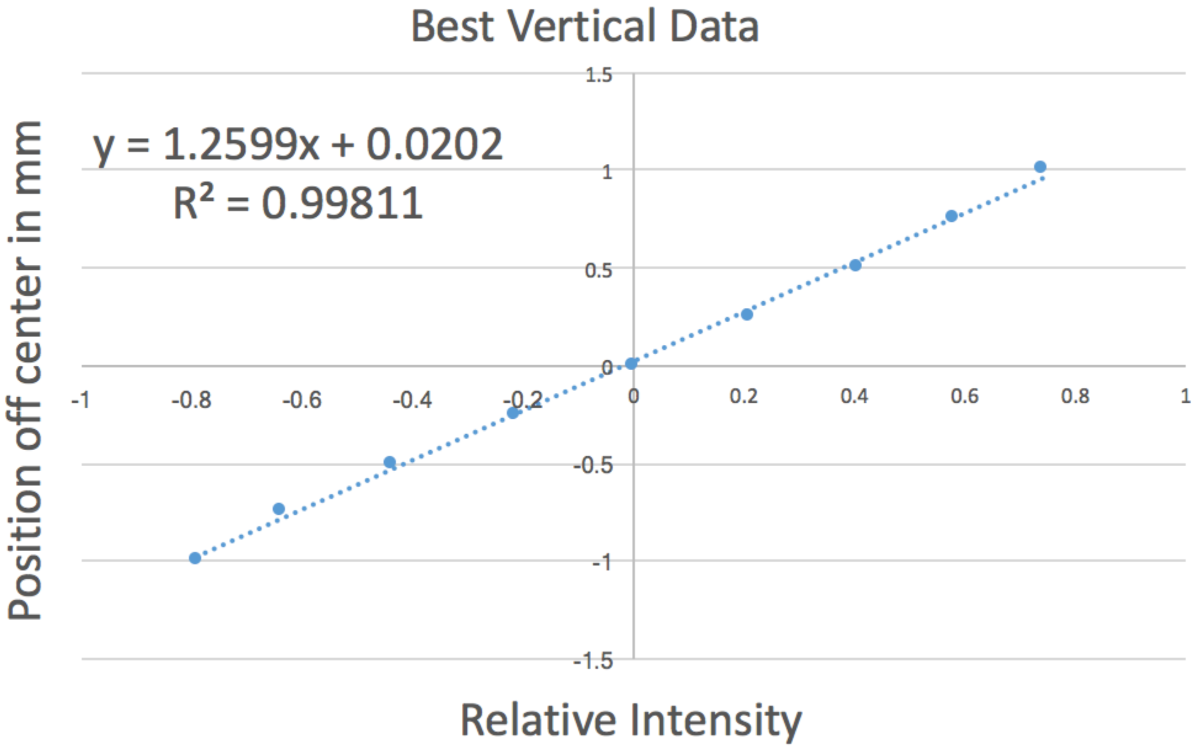

Figure A.6 The final calibration curve for the vertical QPD fit is displayed above.

With the calibration curves now known, the determination of pitch and yaw can be determined as described in chapter 3. The used calibration fit for the QPD are found in figures A.5 and A.6 with values of y = 1.2734 x + 0.047 for the horizontal direction and y = 1.2599 x + 0.0202 for the vertical orientation.

Appendix B: Alignment Procedure

This appendix outlines the steps to roughly align the system, and then fine tune the alignment with a sample alignment procedure. The primary goal of this procedure is to align the laser beam to be parallel to the motion of the translational table. The spot of the laser will move slightly, but with alignment the average will be near zero. Variation of the laser spot is normal and expected due to local tilt inherent to the translational table construction. An iterative technique is used to first roughly align the system, followed by fine tuning adjustments. The tilt that is calculated is dependent on both the deviation of the spot on the QPD and the distance from the laser to the QPD.

Rough Alignment: To roughly align the laser and QPD the translational table should be set to a Z position of 580mm. At this location the photodetector should be translated until both horizontal and vertical outputs from the detector are near zero. These output values range from 0 at center to 1000 at the edge. Once the laser is hitting the target near the center at this location, the position should be translated in steps of 1cm to get a plot of the current alignment. A file is currently loaded on the Pi that serves this purpose, to access it the following commands can be used. This program tells the system to take 4 data points in 1cm increments and average the output.

```
Cd experiment/
Python experiment_2.py mfile
```

At this point the laser should be hitting the photodetector over the entire length of the translational table. The intensity output from the detector should consistently read an intensity of ~1000. If the Intensity drastically dips, or the vertical or horizontal outputs no longer display data, further adjustment of the detector may be required. We have now roughly aligned the system and have a set of data. With these plots we will now finely align the system.

Fine Alignment: To finely align the system an iterative process is needed as can be seen below. To control alignment, we can translate the data up and down (more positive or more negative) by translating the detector. To control the angle or slope of the data we must adjust the pitch and yaw of the laser adjustments. A sample of this iterative process is presented. The first plot demonstrates a roughly aligned system. We note all data is on the scale, and we have no output data pinned on the edge.

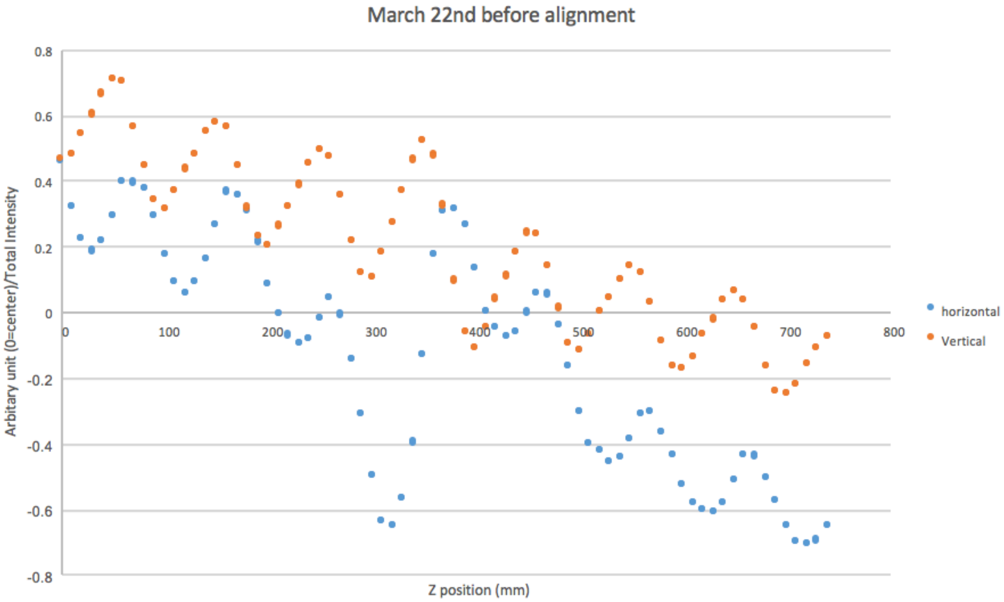

Figure B.1: A plot of a poorly aligned system is seen above. Since all data is on target and not pinned, it is clear the rough alignment was successful. The slope of both vertical and horizontal indicate further fine alignment is required before using the system.

The first set of data seen above is all on scale but has a clear slope to it. To adjust the dataset, the pitch and yaw of the laser were both adjusted by one tick mark. The fine adjustment scales on the laser control range from 0 to 25, the rough alignment scale goes from 0 to 4. The initial positions of the laser were as follows:

Vertical: rough (2 1/4), Fine (22)

Horizontal: rough (2 1/2), Fine (12)

To adjust for the angle both the vertical and horizontal were rotated 1 tick mark on the fine scale, this correlates to a 1/25th of a full turn. The dataset for vertical at 23 and horizontal at 13 is displayed below. It is noted that the slope has decreased as expected, and the data has been shifted in the negative direction. Since the data still has a slope, the pitch and yaw were further adjusted one more tick positive seen in Figure B.3.

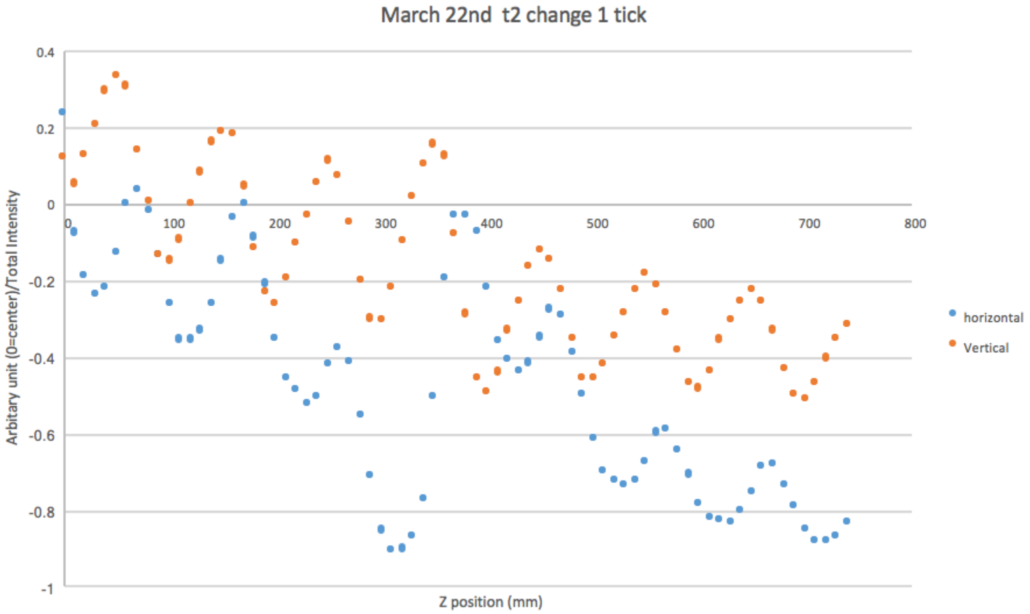

Figure B.2: The slope has decreased when compared to figure B.1, however more fine adjustment is needed to the laser stage to remove the slope.

As can be seen in Figure B.3, further adjusting the vertical and horizontal to new positions at vertical 24 and horizontal at 14 give a more linear trend, however we still see a slight slope. We note here that all of the data has been shifted into the negative region, and thus translation of the detector is required.

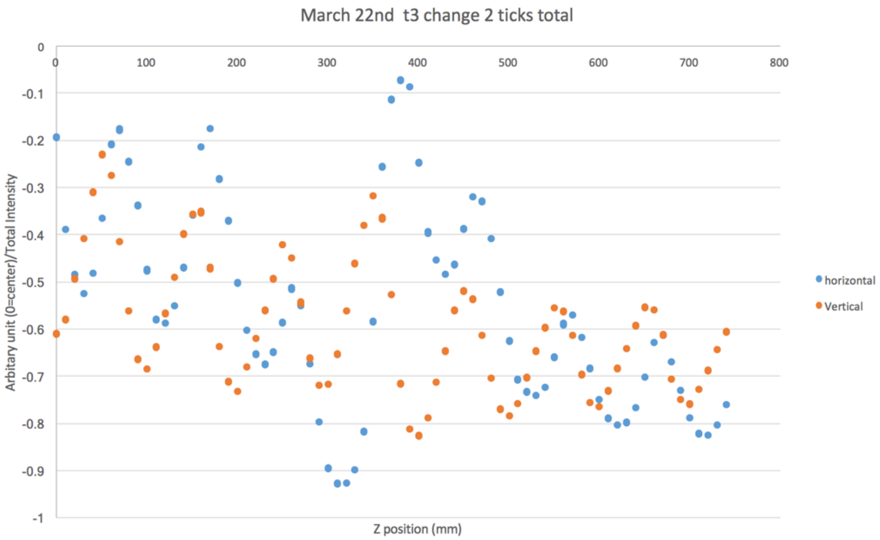

Figure B.3: The slope of the vertical and horizontal has clearly been decreased when compared with figures B.1 and B.2, however they are both now far off center and thus the detector needs to be translated to center both directions. A slight slope still exists here.

After translating the detector, we get an output seen below in Figure B.4. The slope of vertical and horizontal remain the same, they are simply shifted to be more centered around zero. We note we still have a slight slope, so some further adjustment is still required.

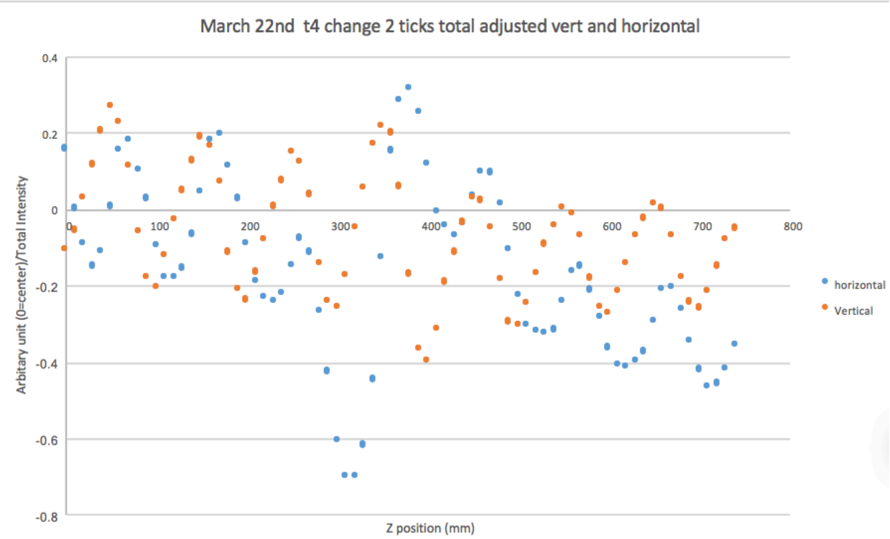

Figure B.4: The plot has now been returned to center by translating the detector, however a slight slope is still detected, so further fine adjustment is required.

The pitch is now adjusted for the laser from 24 to a final vertical pitch position of 0 (as the scale goes from 0 to 24), and the horizontal yaw adjustment from 14 to a final position of 15. We note, as seen below the data was once again shifted in the negative direction, however the slope of both datasets seems rather linear. We also note the horizontal data is pinned around 300 mm in Z.

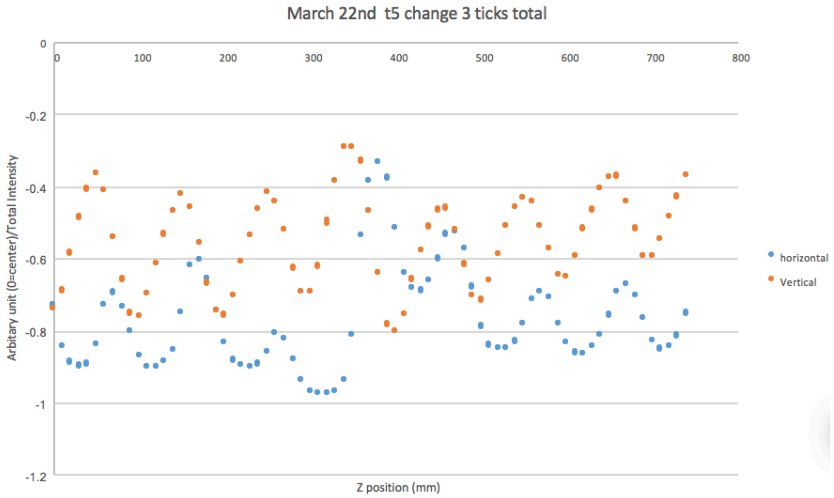

Figure B.5: The slope of both vertical and horizontal are now near zero, it is apparent that both now need to be translated on the detector back to the middle.

To adjust the scale, we once again translate the detector so that both horizontal and vertical are centered around zero. Again, to do this, we pick a spot in Z where the vertical and horizontal should both be near zero, and adjust the detector until both display a value near zero. This adjustment centered the dataset nicely as can be seen below in Figure B.6.

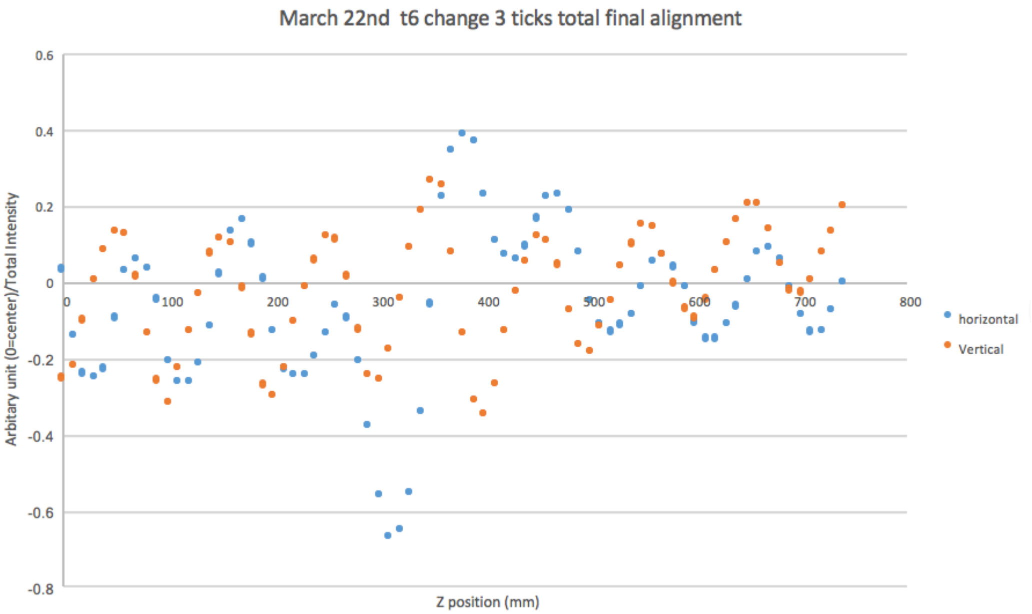

Figure B.6: The final alignment is seen above. Both vertical and horizontal directions have little to no net slope, and they are both centered around 0 on the vertical axis. This is a reproducible trend characteristic of a properly aligned system.

As can be seen above the final dataset looks good. The data is centered around an intensity of 0, and both horizontal and vertical data show little or no slope. After 6 iterations we see the alignment has gone from poorly aligned, to a close to ideal alignment. Each dataset takes about 15 minutes to acquire using this method.

The overall trend for adjusting the pitch and yaw is also clearly seen. As we increase the values of the pitch and yaw adjustment (rotating each clockwise), we see the slope goes from negative to more positive. We note these adjustments are very sensitive, in this sample alignment procedure we went from 22 to 25 on vertical and 12 to 15 on horizontal. These correlate to 3/25ths of a full turn of each of the fine adjustment controls. The translation of the detector is much more course, typically a full turn of translation correlates to a change in intensity of about 200 (on a scale from 0 to 1000). For more information on the calibration and adjustment of the quadrant photodetector see Appendix A.

Appendix C: Electrical Connections

The purpose of this appendix is simply to show a block diagram for the electrical components of the alignment device. The DB9 cable is used to power and take data from the photodetector. The Raspberry Pi is used to control the translational and rotation stages of the alignment device, as well as to capture images of the roll inherent to the system.

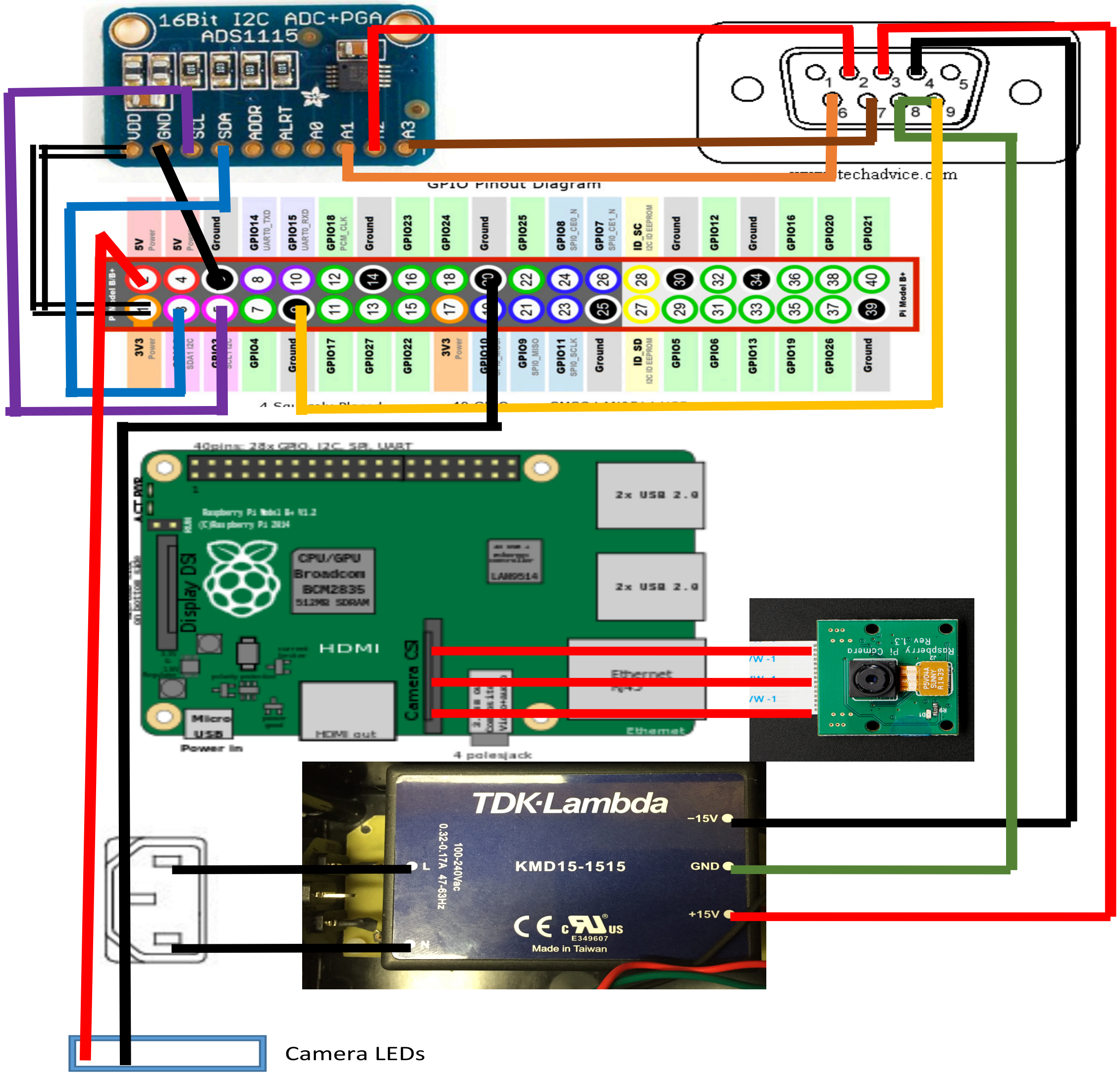

Figure C.1: A block diagram of the electrical connections for the Raspberry Pi and related electrical connections is displayed above. Not displayed is the single USB connection from the Raspberry Pi to the translational and rotational stage controller box. The TDK-Lambda device provides power to the quadrant photodetector, connected with the DB9 cable. The I2C device collects data from the photodetector output and relays the information to the Pi.

Device	Device Pin	Wire color	Destination	Destination pin
Pi	1	White	I2C	1 (VDD)
Pi	2	Red	Camera LED	N/A
Pi	3	Blue	I2C	4 (SDA)
Pi	5	Purple	I2C	3 (SCL)
PI	6	Black	IC2	2 (GND)
Pi	9	Yellow	DB9	9
Pi	20	Black	Camera LED	N/A
I2C	1(VDD)	White	Pi	1
I2C	2(GND)	Black	Pi	6
I2C	3(SCL)	Purple	Pi	5
I2C	4(SDA)	Blue	Pi	3
I2C	8(A1)	Orange	DB9	6
I2C	9(A2)	Red	DB9	2
I2C	10(A3)	Brown	DB9	7
KMD15-1515	-15V	Black	DB9	4
KMD15-1515	+15V	Red	DB9	3
KMD15-1515	GND	Green	DB9	8 and 9 (Pi GND)
DB9	2	Red	I2C	9 (A2)
DB9	3	Red	TDK 1515	+15V
DB9	4	Black	TDK 1515	-15V
DB9	6	Orange	I2C	8(A1)
DB9	7	Brown	IC2	10(A3)
DB9	8	Green	TDK 1515	GND
DB9	9	Yellow	Pi	9
Camera LED	N/A	Red	Pi	2
Camera LED	N/A	Black	Pi	20

Table C.1: A summary of electrical connections is presented above for reference use.

Appendix D: Detailed Drawings

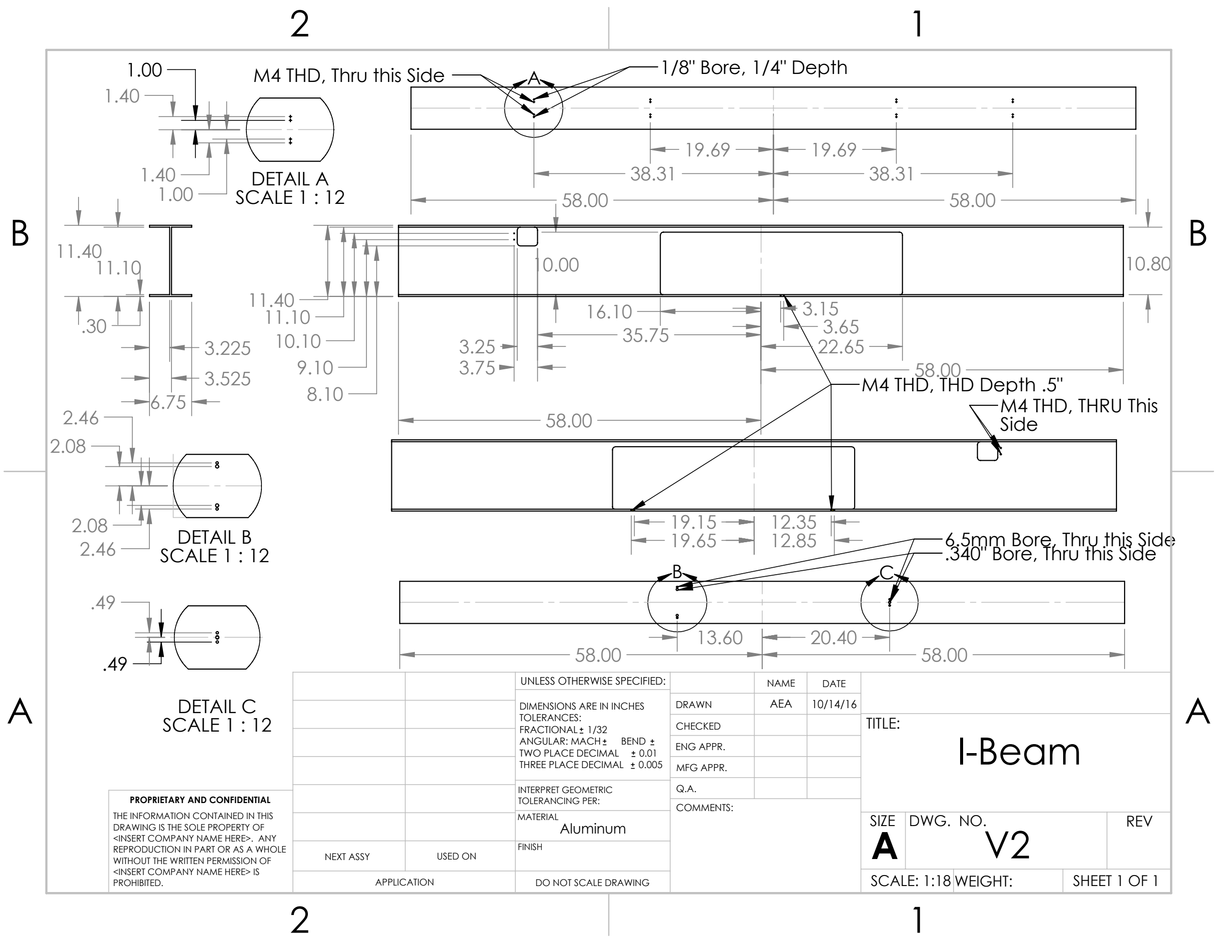

Figure D.1: The specifications of our I beam, used to support our translational radioactive alignment device can be seen above. The translational table is mounted in the large cutout near the center. The four quadrant photodetector is housed near the small cutout. All units are in inches. The mounting holes for the translational table can be seen in Detail A, B, and C. We mount the translational table using one M4 bolt at one end in the center of the stage, and two M4s on the other end. We have also allowed for adjustment feet to be used as well seen with the eighth inch bore holes, again using a three-point suspension system.

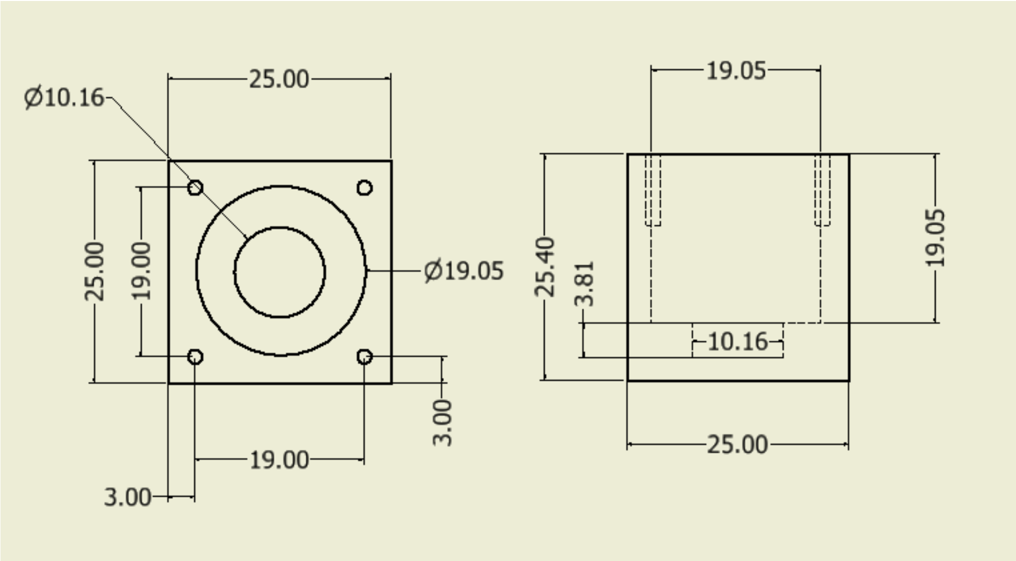

Figure D.2: The dimensions of our second collimator can be seen above. This device houses a lead cylinder that holds our radioactive source. A bracket and mounting system have been built that allow this second collimator to be placed outside the LXe. The second collimator can then be used to test one MPPC at a time, and be translated across the array. This device acts as a crosscheck of our much larger translational alignment device. The collimator housing may be surveyed to determine the precise location of the beam spot. The small cutout in the base, seen on the right is used as an endcap to the device and holds a piece of lead, this way when it is not in use the radioactive source is contained.

Figure D.3: The mounting brackets used to support the collimator can be seen above.

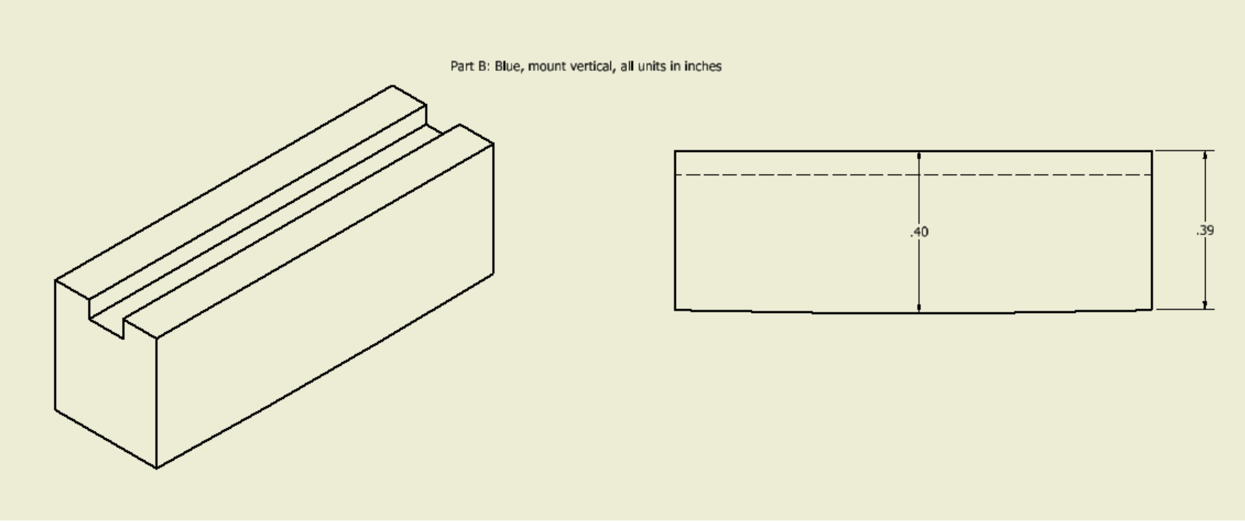

Part B: Blue, mount vertical, all units in inches

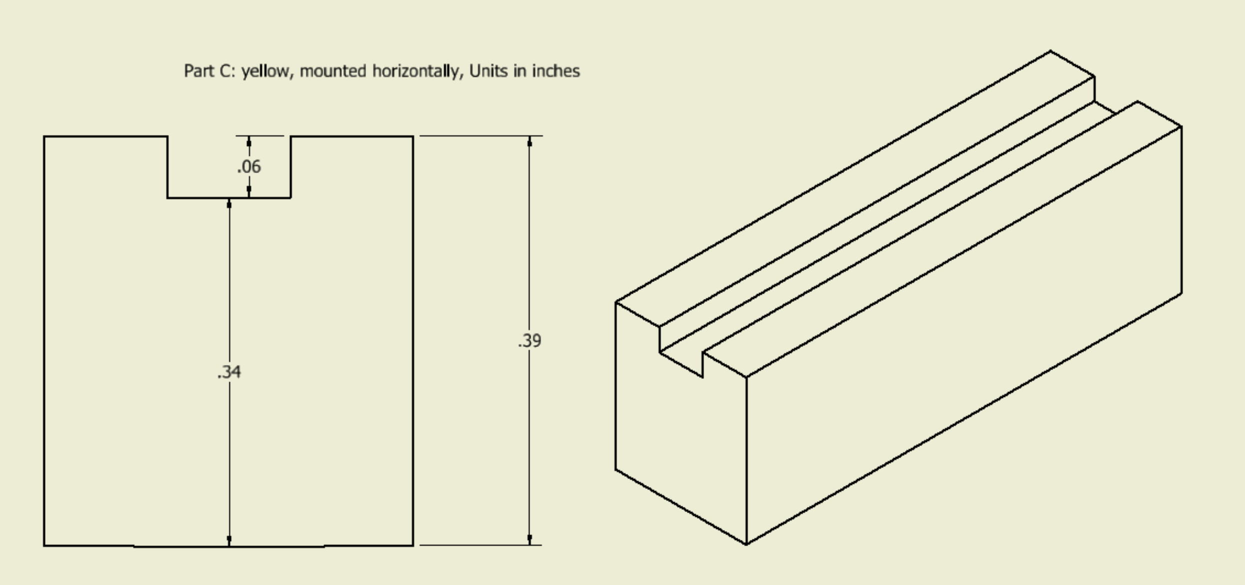

Part C: yellow, mounted horizontally, Units in inches

Figure D.4: The specifications for the lead attenuation devices can be seen above. The width of the lead placed in the holder is 0.125” and it is located at the center of the holder. The slight curvature of the base is to conform to the curved outer wall of the LXe.

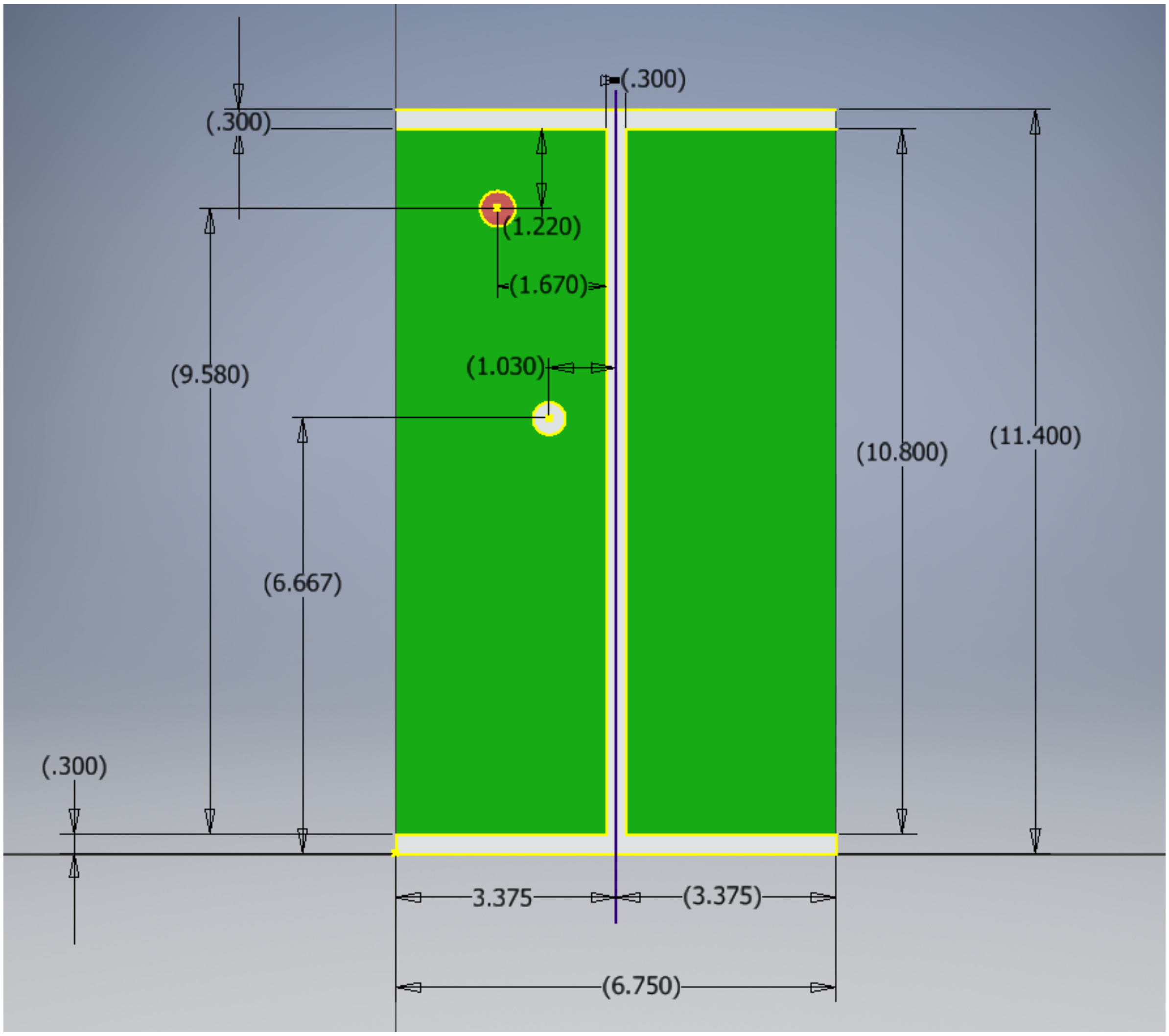

Figure D.5: The location of the laser line, seen in red, and the collimator line seen in grey are noted above.

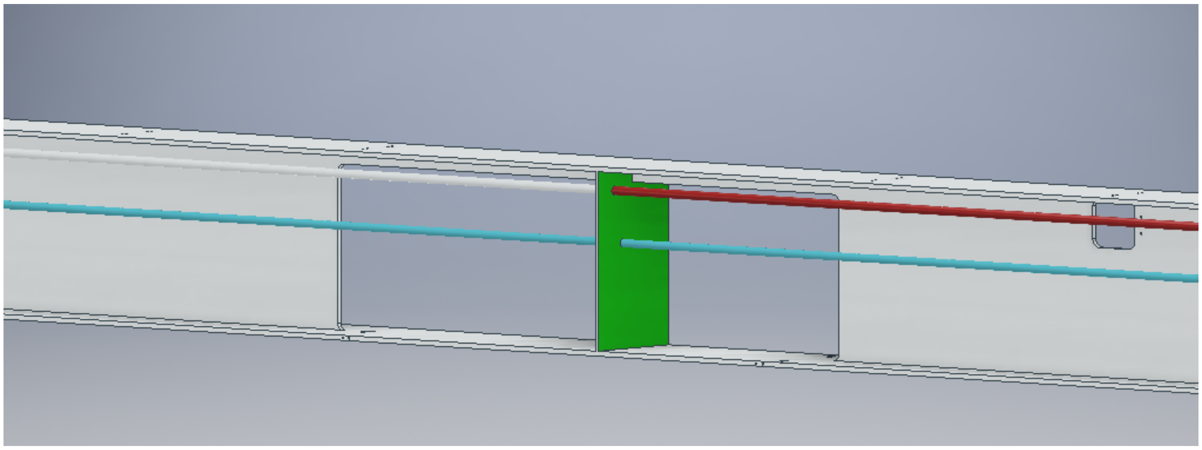

Figure D.6: An angled view of the laser line (red) and collimator line (blue) can be seen above for reference.

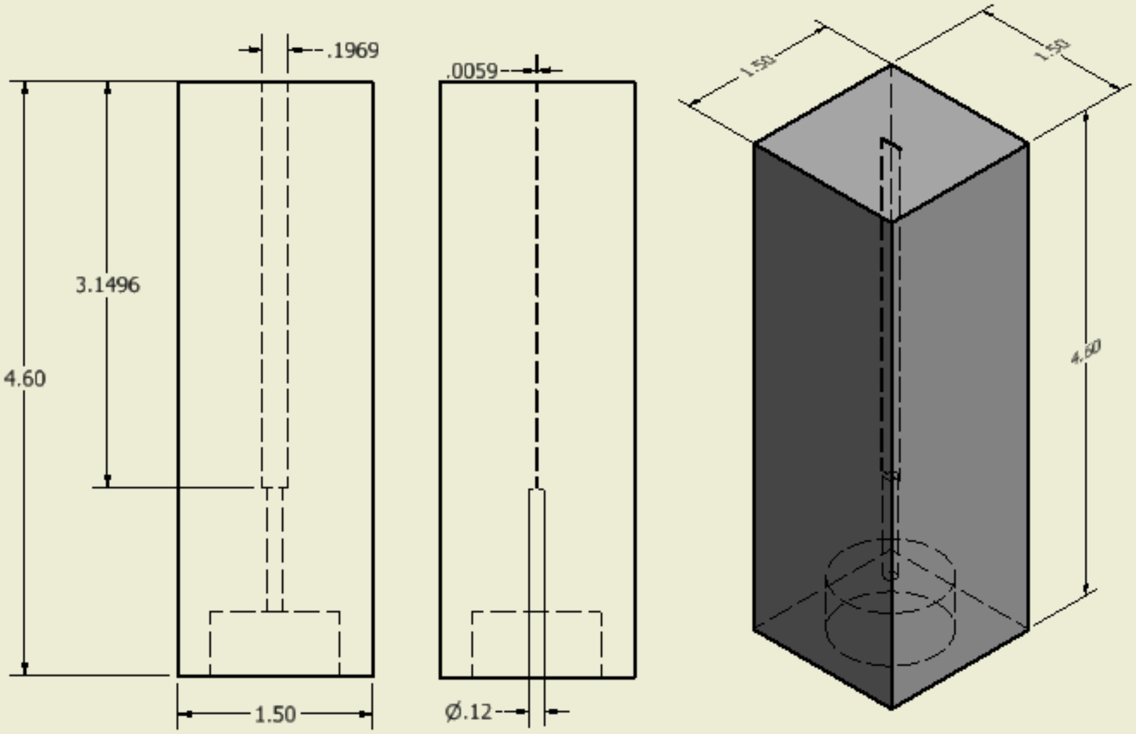

Figure D.7: The dimensions of the brass collimator used at PSI are displayed above, all units are in inches. The radioactive cobalt source is a cylinder with dimensions of 0.12” diameter and is 0.42” long. The source sits near the bottom of the collimator.

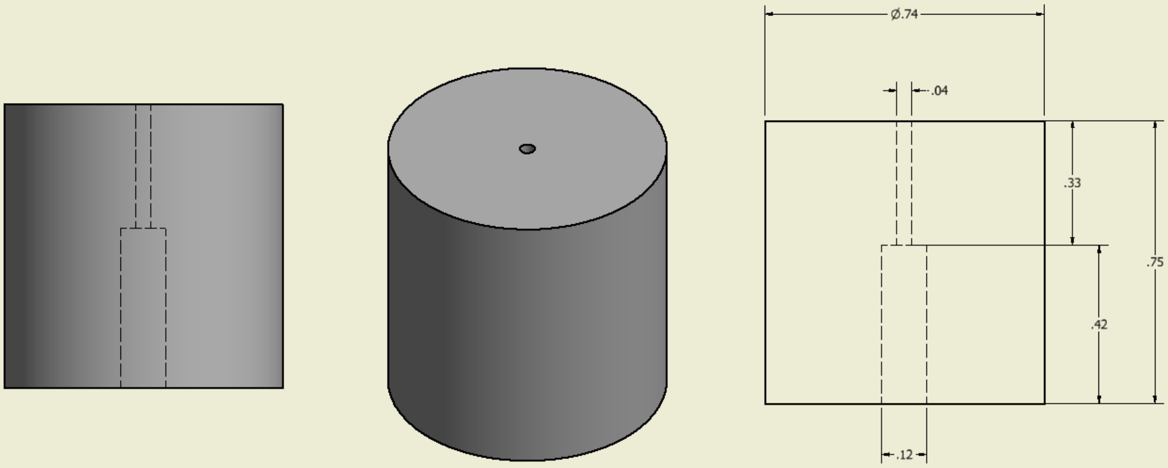

Figure: D.8: The secondary collimator used at PSI was fabricated from lead, with dimensions displayed above in inches. The cobalt source sits in the larger pocket at the bottom of the collimator.

Bibliography

[1] E. Ripiccini, New results from the MEG Experiment at PSI and the MEG upgrade (2015) https://doi.org/10.1016/j.nuclphysbps.2015.02.031

[2] A.M. Baldini et al. Search for the Lepton Flavour Violating Decay $\mu^+ \Rightarrow e^+\ \gamma$ with the Full Dataset of the MEG II Experiment (2016) arXiv:1605.05081v3

[3] Angela Papa, The MEG/MEGII and Mu3e experiments at PSI (2015) https://www.mpi-hd.mpg.de/WIN2015/talks/flavour2_papa.pdf

[4] A. M. Baldini et al. MEG Upgrade Proposal (2013) arXiv:1301.7225v2

[5] J. Adam et al. New Analysis Method to Confirm the Upper Limit of the Branching Ratio B (μ+ → e+ + γ) from the MEG Experiment (2012) http://e-collection.library.ethz.ch/eserv/eth:6366/eth-6366-02.pdf

[6] Boehm, F., & Vogel, P. (1992). *Physics of Massive Neutrinos*. Cambridge: Cambridge University Press. doi:10.1017/CBO9780511622571

[7] R. Barbieri, L. J. Hall, A. Strumia, Violations of lepton flavor and CP in supersymmetric unified theories, Nucl.Phys. B445 (1995) 219–251. arXiv:hep-ph/9501334.

[8] J. Hisano, D. Nomura, T. Yanagida, Atmospheric neutrino oscillation and large lepton flavor violation in the SUSY SU(5) GUT, Phys.Lett. B437 (1998) 351–358. arXiv:hep-ph/9711348.

[9] M. Raidal, A. van der Schaaf, I. Bigi, M. Mangano, Y. K. Semertzidis, et al., Flavour physics of leptons and dipole moments, Eur.Phys.J. C57 (2008) 13–182. arXiv:0801.1826.

[10] G. Blankenburg, G. Isidori, J. Jones-Perez, Neutrino Masses and LFV from Minimal Breaking of U(3)5 and U(2)5 flavor Symmetries, Eur.Phys.J. C72 (2012) 2126. arXiv:1204.0688.

[11] J. Beringer et al. (Particle Data Group) (2012). "PDGLive Particle Summary 'Leptons (e, mu, tau, ... neutrinos ...)'" (PDF). Particle Data Group. Retrieved 2013-01-12.

[12] Yusuke Uchiyama. Analysis of the First MEG Physics Data to Search for the Decay μ+ → e+γ. Department of Physics, School of Science, the University of Tokyo (2009)

[13] W. Ootani et al., Development of a thin-wall superconducting magnet for the positron spectrometer in the MEG experiment. IEEE Trans. Appl. Supercond. 14(2), 568–571 (2004). doi: 10.1109/TASC.2004.829721

[14] M. De Gerone et al., Development and commissioning of the Timing Counter for the MEG Experiment. IEEE Trans. Nucl. Sci. 59, 379–388 (2012). doi:10.1109/TNS.2012.2187311, arXiv:1112.0110

[15] M. De Gerone et al., The MEG timing counter calibration and performance. Nucl. Instrm. and Meth. A 638, 41–46 (2011). doi: 10.1016/j.nima.2011.02.044

[16] M. Hildebrandt, The drift chamber system of the MEG experiment. Nucl. Instrm. and Meth. A 623(1), 111–113 (2010). doi: 10.1016/j.nima.2010.02.165

[17] R. Sawada, Performance of liquid xenon gamma ray detector for MEG. Nucl. Instrm. and Meth. A 623(1), 258–260 (2010). doi: 10.1016/j.nima.2010.02.214

[18] A. Baldini et al., Absorption of scintillation light in a 100 l liquid xenon γ-ray detector and expected detector performance. Nucl. Instrm. and Meth. A 545(3), 753–764 (2005). doi:10.1016/j. nima.2005.02.029, arXiv:0407033

[19] J. Adam, X. Bai, A. Baldini, E. Baracchini, C. Bemporad, et al., The MEG detector for μ+ → e+γ decay search, Eur.Phys.J. C73 (4) (2013) 2365. arXiv:1303.2348.

[20] H. Anderhub, M. Backes, A. Biland, A. Boller, I. Braun, et al. FACT – the First Cherenkov Telescope using a G-APD Camera for TeV Gamma-ray Astronomy (HEAD 2010). Nucl.Instrum.Meth., A639:58–61, 2011.

[21] FARO portable coordinate measuring machines. http://www.faro.com/en-us/products

[22] L. E. Diaz. "Cobalt-57: Production". *JPNM Physics Isotopes*. University of Harvard. Retrieved 2013-11-15.

[23] E. Aprile and T. Doke, “Liquid Xenon Detectors for Particle Physics and Astrophysics”, arXiv:0910.4956v1 [hep-ex] (2009).

[24] K. Ozone, “Liquid Xenon Scintillation Detector for the New μ → eγ Search Experiment”, Ph.D. Thesis, the University of Tokyo (2005), http://meg.web.psi.ch/ docs/theses/ozoned.pdf/.

[25] R. Sawada, “A Liquid Xenon Scintillation Detector to Search for the Lepton Flavor Violating Muon Decay with a Sensitivity of 10−13”, Ph.D. Thesis, the University of Tokyo (2008), http://meg.web.psi.ch/docs/theses/sawada phd.pdf/.

[26] A. Baldini et al., “A radioactive point-source lattice for calibrating and monitoring the liquid xenon calorimeter for the MEG experiment”, Nucl. Instr. Meth. A, 565, 589-598 (2006).

[27] S. Himi et al., “Liquid and Solid Argon, and Nitrogen-doped liquid and solid Argon Scintillators”, Nucl. Inst. Meth. 203, 153 (1982).

[28] S. Mihara et al., “Development of a method for liquid xenon purification using a cryogenic centrifugal pump”, Cryogenics 46 688-693 (2006).

[29] Quadrant Silicon Photodiode Operation http://www.osioptoelectronics.com/application-notes/AN-Quadrant-Silicon-Photodiode-Operation-Guide.pdf

[30] DRS4 Evaluation Board. https://www.psi.ch/drs/evaluation-board

[31] The WaveDAQ SYSTEM FOR THE MEG II UPGRADE. https://www.psi.ch/drs/DocumentationEN/elba15.pdf

[32] J. Adam et al. New limit on the lepton-flavour violating decay $\mu^+ \rightarrow e^+\gamma$. Phys. Rev. Lett., 107:171801, 2011.